J. Fluid Mech. (2005), *vol.* 528, *pp.* 53–86.
doi:10.1017/S002211200400309X Printed in the United Kingdom

Unsteady bubble propagation in a flexible channel: predictions of a viscous stick-slip instability

By DAVID HALPERN[1], SHAILESH NAIRE[2]†, OLIVER E. JENSEN[2] AND DONALD P. GAVER III[3]

[1]Department of Mathematics, University of Alabama, Tuscaloosa, AL 35487, USA
[2]School of Mathematical Sciences, University of Nottingham, University Park, NG7 2RD, UK
[3]Department of Biomedical Engineering, Tulane University, New Orleans, LA 70118, USA

(Received 11 March 2004 and in revised form 15 June 2004)

We investigate the unsteady motion of a long bubble advancing under either prescribed pressure p_b or prescribed volume flux q_b into a fluid-filled flexible-walled channel at zero Reynolds number, an idealized model for the reopening of a liquid-lined lung airway. The channel walls are held under longitudinal tension and are supported by external springs; the bubble moves with speed U. Provided p_b exceeds a critical pressure p_{crit}, the system exhibits two types of steady motion. At low speeds, the bubble acts like a piston, slowly pushing a column of fluid ahead of itself, and U decreases with increasing p_b. At high speeds, the bubble rapidly peels the channel walls apart and U increases with increasing p_b. Using two independent time-dependent simulation techniques (a two-dimensional boundary-element method and a one-dimensional asymptotic approximation), we show that with prescribed $p_b > p_{crit}$, peeling motion is stable and the steady pushing solution is unstable; for $p_b < p_{crit}$ the system ultimately exhibits unsteady pushing behaviour for which U continually diminishes with time. When q_b is prescribed, peeling motion (with large q_b) is again stable, but pushing motion (with small q_b) loses stability at long times to a novel instability leading to spontaneous relaxation oscillations of increasing amplitude and period, for which the bubble switches abruptly between slow unsteady pushing and rapid quasi-steady peeling. This stick–slip motion is characterized using a third-order lumped-parameter model which in turn is reduced to a nonlinear map. Implications for the inflation of occluded lung airways are discussed.

1. Introduction

The lung consists of a network of bifurcating flexible airways that conduct air between the mouth and the alveoli, the site of gas exchange with blood. The thin liquid lining of the airways plays an important role in determining the airways' mechanical properties and stability (Grotberg 1994). It does so via capillary forces arising from surface tension acting at the air–liquid interface. These forces are mediated by naturally produced pulmonary surfactant, which lowers surface tension, thereby improving overall lung compliance and enhancing airway stability. When infants are born prematurely the immaturity of the surfactant system can lead to respiratory distress syndrome (RDS), which is characterized by large regions of atelectatic (closed)

† Present address: Department of Mathematics, Heriot-Watt University, Riccarton, Edinburgh EH14 4AS, UK.

airways; these can be opened clinically using mechanical ventilation and surfactant replacement therapy (SRT). Although SRT has been used routinely since the 1990s and has dramatically reduced the mortality of RDS, this disease remains the fourth leading cause of death of premature infants in the United States (Guyer *et al.* 1999) and is a cause of long-term lung damage in surviving infants. A related condition in adults is acute respiratory distress syndrome (ARDS), which can follow insults such as systemic infection (sepsis), smoke inhalation or radiation poisoning. Here a flux of liquid into airspaces leads to pulmonary oedema, alveolar flooding and surfactant inactivation by proteins that escape from the vasculature into airways. In both forms of RDS, airways can become blocked with liquid, either through liquid-plug formation arising via a Rayleigh–Plateau (surface-tension-driven) instability of the airway liquid lining (Kamm & Schroter 1989; Johnson *et al.* 1991; Halpern & Grotberg 1992), or through airway collapse induced by low liquid capillary pressures (Rosenzweig & Jensen 2002; Heil & White 2002), or through a combination of both mechanisms (Heil 1999*a*, *b*).

The process whereby an occluded airway is reopened is thus of fundamental importance in the treatment and progression of obstructive pulmonary diseases including asthma, cystic fibrosis and RDS. It is also a key feature of the first breath of a newborn infant, where air must be drawn rapidly into initially liquid-filled airways. In general, reopening arises either through the displacement and rupture of short liquid plugs (Howell, Waters & Grotberg 2000) or through the inflation of an initially flooded and collapsed airway (Gaver III, Samsel & Solway 1990). A number of important physiological issues are related to the associated interactions between airway liquid and deformable airway walls (Grotberg 2001; Gaver III, Jensen & Halpern 2005). These interactions span many length and time scales. At the organ level, airway closure may result in abnormal pulmonary mechanical behaviour due to regional compliance mismatch. This can result in local regions of airway and alveolar distension and hyperventilation of open regions of the lung, while neighbouring closed regions receive little or no gas exchange. At the cellular level, the process of reopening collapsed airways can wound the lung by stretching sensitive alveolar tissue (Savla, Sporn & Waters 1997; Tschumperlin, Oswari & Margulies 2000). In addition, interfacial stresses during reopening can damage airway epithelial cells (Bilek, Dee & Gaver 2003). This damage appears to result from large normal-stress gradients that propagate across the cells. At the molecular level, the stability of airways and the stress magnitudes during reopening are directly related to the molecular properties of surfactant, including the rates of surfactant sorption and the interaction between surfactant lipids and proteins (Notter 2000).

In this paper we focus on the stability of airway reopening, using a system in which an airway is modelled as a planar flexible-walled channel, as illustrated in figure 1 (and outlined in detail in § 2 below). The initially liquid-filled channel is confined by two flexible membranes held under large longitudinal tension $\eta^\star$ and supported externally by linearly elastic springs with stiffness $\Gamma^\star$. The channel width under stress-free conditions is $2H^\star$. The liquid within the channel is assumed to be Newtonian with constant viscosity $\mu^\star$ and uniform surface tension $\gamma^\star$. The channel is inflated by blowing a bubble of air into one end of the channel with either a prescribed pressure $p_b^\star$ or a prescribed volume flux $q_b^\star$ per unit width such that the bubble tip advances with speed $U^\star(t^\star)$ at time $t^\star$.

Gaver III *et al.* (1996) showed theoretically that steady bubble propagation in this system can occur provided the scaled bubble pressure $p_b = p_b^\star/(\gamma^\star/H^\star)$ exceeds a critical value, p_{crit}, dependent on material parameters and geometry. Corresponding to this minimum pressure is a dimensionless critical speed $U_{crit} = \mu^\star U_{crit}^\star/\gamma^\star$ (a capillary

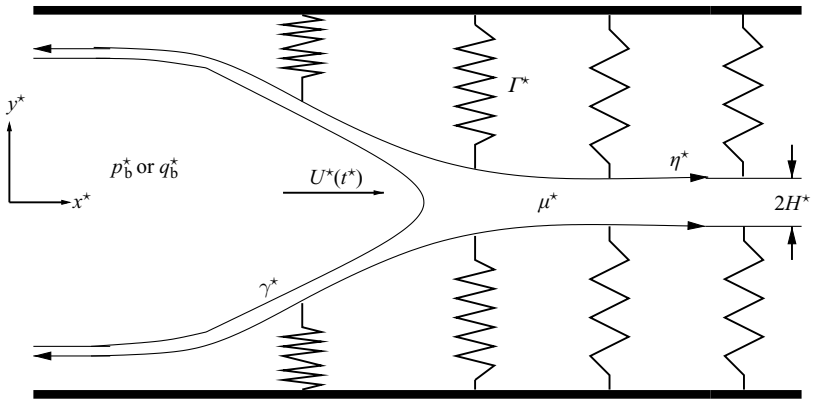

FIGURE 1. Schematic of physical model: a bubble of air propagates from left to right, inflating the liquid-filled channel.

number representing the ratio of viscous to surface-tension forces). For $p_b > p_{crit}$ there are two steady solution branches (see figure 2*a*): one for $U = \mu^\star U^\star/\gamma^\star < U_{crit}$ along which U decreases as p_b increases; one for $U > U_{crit}$ along which U increases with p_b. On the lower branch (with $U < U_{crit}$), the nearly circular bubble tip displaces a long column of fluid ahead of itself between almost parallel membranes: this is therefore referred to as the 'pushing' branch. Using Bretherton's (1961) analysis of the steady low-capillary-number motion of a bubble through a circular tube, Gaver III *et al.* (1996) showed that on this branch $p_b \sim \Gamma U^{-2/3}$ as $U \to 0$, where $\Gamma = \Gamma^\star H^{\star 2}/\gamma^\star$ is a dimensionless membrane stiffness. On the upper steady solution branch ($U > U_{crit}$ in figure 2*a*), as U and p_b increase the bubble tip becomes more pointed and the membrane walls are more tapered in the tip region. Asymptotic analysis in the limit of large membrane tension (with $\eta = \eta^\star/\gamma^\star \gg 1$) and weak springs shows that on this 'peeling' branch $p_b \sim \eta^{1/6}\Gamma^{1/2}U^{1/3}$ (Jensen *et al.* 2002). Computations of this solution branch obtained using two-dimensional computational simulations and a one-dimensional asymptotic analysis assuming $\eta \gg 1$ both show good agreement with Perun & Gaver's (1995*b*) experimental measurements of steady peeling behaviour (Jensen *et al.* 2002).

These two distinct steady reopening responses are robust to variations in modelling assumptions, persisting for example in three dimensions (Hazel & Heil 2003) and in the presence of surfactant (Yap & Gaver 1998). Qualitatively new behaviour arises only at very low speeds when membrane walls are weakly permeable (Jensen & Horsburgh 2004) or at high speeds when fluid inertia (Heil 2000) and viscoelasticity (Hsu, Strohl & Jamieson 1994) are significant. Peeling but not pushing behaviour has been observed experimentally, suggesting that the pushing branch may be unstable under certain conditions. Furthermore, a transient overshoot in $p_b^\star$ was observed when reopening was initiated at constant bubble flux $q_b^\star$ (Perun & Gaver 1995*a*, *b*), and Perun & Gaver (1995*a*) reported difficulties in obtaining steady reopening at low $q_b^\star$. While the mechanism of transient overshoot has recently been captured using a one-dimensional asymptotic model (Horsburgh 2000; Naire & Jensen 2003), the stability of the two solution branches under different reopening conditions has yet to be fully explored. Furthermore, experiments in lungs indicate avalanche behaviour (Suki *et al.* 1994) that may be a result of flow instability (Alencar *et al.* 2002). The use of noise to spawn such instabilities has been suggested as a means for increasing ventilator efficacy (Suki *et al.* 1998).

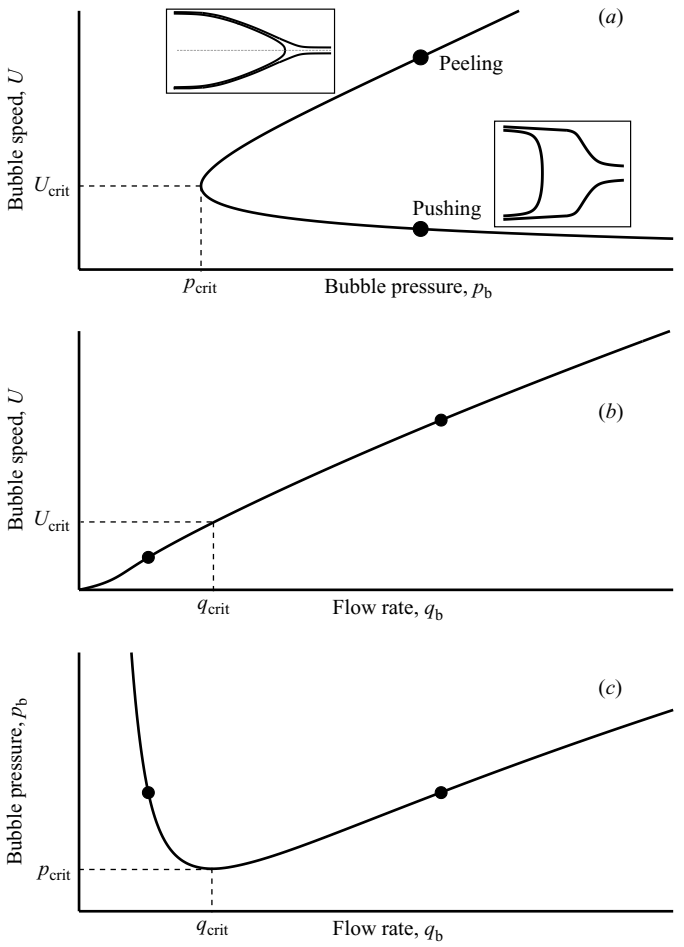

FIGURE 2. Steady solution branches, plotted in (*a*) the (p_{b}, U)-plane, (*b*) the (q_{b}, U)-plane and (*c*) the $(q_{\mathrm{b}}, p_{\mathrm{b}})$-plane. Black circles in each panel show two steady solutions with the same p_{b}, one on the pushing branch and the other on the peeling branch. Insets in (*a*) show characteristic shapes of pushing and peeling solutions.

The aim of the present paper is therefore to investigate the stability of pushing and peeling motions under conditions of either prescribed bubble pressure or prescribed bubble flux. We use two complementary time-dependent techniques (outlined in § 3): a computational two-dimensional Stokes-flow simulation based on the boundary-element method, and a one-dimensional asymptotic model valid when membrane slopes are uniformly small. The two methods allow for cross-validation and provide flexibility in examining detailed flow structures and in integrating over long time intervals. By subjecting typical pushing and peeling steady-state solutions (the black circles on figure 2*a*) to small, prescribed variations in bubble pressure and allowing U to vary, we will confirm (in § 4.1, following preliminary calculations by Horsburgh 2000) Gaver III *et al.*'s (1996) conjecture that the pushing branch is unstable to small perturbations in speed with $p_{\mathrm{b}}^{\star}$ held fixed, and that the peeling branch is stable. The pushing branch loses stability to a direct (zero-frequency) instability, resulting either in steady peeling motion or a new form of unsteady pushing motion for which $U^{\star} \to 0$

as $t^\star \to \infty$. We demonstrate also how unsteady pushing behaviour ultimately arises when p_b is held fixed at a value below p_crit.

Because of its relevance to experiment and to clinical ventilation protocols, we then consider (in § 4.2) the stability of the two solution branches when the bubble volume flux $q_\mathrm{b}^\star$ is prescribed, taking $q_\mathrm{b} = q_\mathrm{b}^\star \mu/(\gamma H^\star)$ as a dimensionless control parameter. Under steady conditions $q_\mathrm{b} \approx p_\mathrm{b} U/\Gamma$, since the bubble has approximate width p_b/Γ at its upstream end and propagates with speed U. The two steady solution branches are therefore single-valued in the (q_b, U)- and $(q_\mathrm{b}, p_\mathrm{b})$-planes (figure 2*b*, *c*), with $U \propto q_\mathrm{b}^3$ and $p_\mathrm{b} \propto q_\mathrm{b}^{-2}$ for small q_b (pushing) and $U \propto q_\mathrm{b}^{3/4}$ and $p_\mathrm{b} \propto q_\mathrm{b}^{1/4}$ for large q_b (peeling). These single-valued solution branches give no obvious indication of any direct instabilities when q_b is a control parameter. However we find that at low q_b the system exhibits a novel and unexpected instability resulting in growing oscillations. These develop increasingly large amplitude, with alternating pushing and peeling motion leading to abrupt and non-periodic variations in bubble pressure and bubble speed. The mechanism of the instability is clarified using a third-order (lumped-parameter) ODE model in § 5, which characterizes some of the more striking features of this dynamical system. In particular, we show that the primary instability is not (as might be expected) a Hopf bifurcation, but is instead a dynamic bifurcation of a time-dependent state, and that large-amplitude oscillations exhibit a self-similar structure. The relevance of this instability to airway reopening is discussed in § 6.

2. Model formulation

We consider a model similar to that treated by Gaver III *et al.* (1996) and Jensen *et al.* (2002), as illustrated in figure 1. The channel is inflated by a bubble of incompressible, inviscid gas that is forced into the channel with either prescribed pressure $p_\mathrm{b}^\star$ or prescribed volume flux $q_\mathrm{b}^\star$ per unit width. Gravitational and inertial effects in the liquid are assumed to be negligible. In a laboratory frame of reference, we introduce Cartesian coordinates $(x^\star, y^\star)$ with $x^\star$ increasing in the direction of the moving bubble, $y^\star = 0$ on the channel centreline and the origin fixed far to the left of the moving bubble tip, which lies at $x^\star = L_\mathrm{b}^\star(t^\star)$. Relative to these axes, the membranes lie at $y^\star = \pm h^\star(x^\star, t^\star)$ and the air–liquid interface lies at $y^\star = \pm f^\star(x^\star, t^\star)$ in $0 \leqslant x^\star \leqslant L_\mathrm{b}^\star(t^\star)$. The flow is assumed to be symmetric about $y^\star = 0$. Far ahead of the bubble tip (as $x^\star \to \infty$), $h^\star \to H^\star$, the springs are unstressed and the liquid is stationary relative to the membranes.

Non-dimensional variables (without stars) are defined with respect to a length $H^\star$, a pressure $\gamma^\star/H^\star$, a speed $\gamma^\star/\mu^\star$ and a time $H^\star\mu^\star/\gamma^\star$. This yields the following parameters:

$$\Gamma = \frac{\Gamma^\star H^{\star 2}}{\gamma^\star}, \quad \eta = \frac{\eta^\star}{\gamma^\star}, \quad p_\mathrm{b} = \frac{p_\mathrm{b}^\star H^\star}{\gamma^\star}, \quad q_\mathrm{b} = \frac{q_\mathrm{b}^\star \mu^\star}{\gamma^\star H^\star}, \tag{2.1}$$

which define the dimensionless spring stiffness, membrane tension, bubble pressure and bubble flux respectively. The dimensionless speed of the bubble satisfies $U(t) = L_{\mathrm{b}t}$. In the following, subscripts x, y and t denote derivatives.

The Stokes and continuity equations for the liquid are given by

$$\nabla \cdot \boldsymbol{u} = 0, \quad \nabla p = \nabla^2 \boldsymbol{u}, \tag{2.2}$$

where $\boldsymbol{u} = (u, v)$ is the dimensionless fluid velocity and p the pressure. The stress and kinematic boundary conditions at the air–liquid interface are

$$\boldsymbol{\tau} \equiv \boldsymbol{\sigma} \cdot \boldsymbol{n} = -(p_\mathrm{b} + \kappa_\mathrm{i})\boldsymbol{n}, \quad f_t = v - u f_x \quad \text{on} \quad y = f(x, t), \tag{2.3}$$

where $\boldsymbol{n}$ is the unit normal pointing out of the liquid, $\boldsymbol{\sigma} = -p\boldsymbol{I} + \nabla\boldsymbol{u} + \nabla\boldsymbol{u}^T$ is the stress tensor and $\kappa_{\mathrm{i}} = f_{xx}/(1+f_x^2)^{3/2}$ is the interfacial curvature. At the flexible wall, the stress and the kinematic boundary conditions are

$$\boldsymbol{m}\cdot\boldsymbol{\sigma}\cdot\boldsymbol{e}_y = \eta\kappa_{\mathrm{m}} m_y - \Gamma(h-1), \quad u = 0, \quad v = h_t \quad \text{on} \quad y = h(x,t). \tag{2.4}$$

Here $\boldsymbol{m} = (m_x, m_y)$ is the unit normal facing out of the liquid and $\kappa_{\mathrm{m}} = h_{xx}/(1+h_x^2)^{3/2}$ is the membrane curvature. The vertical component of the fluid stress is balanced by membrane tension and elastic forces due to the springs. In this model, we assume that any shear-stress-induced or stretch-induced variations in membrane tension are negligible compared to the mean value, as justified by Gaver III *et al.* (1996). Since the membranes move only vertically (2.4*b*, *c*), the springs provide a stress only in the vertical direction. These assumptions follow closely those used in Gaver III *et al.* (1996) and Jensen *et al.* (2002). As we shall see in § 3.3, the small change in the wall kinematic boundary condition due to the small-slope approximation nearly replicates the steady solutions of Gaver III *et al.* (1996). Furthermore, this model captures the behaviour seen in studies using more sophisticated wall models (Heil 2000; Hazel & Heil 2003).

Along $y = 0$ ahead of the bubble tip ($x > L_{\mathrm{b}}$) we have the symmetry conditions

$$u_y = 0 \quad \text{and} \quad v = 0. \tag{2.5}$$

Far ahead of the bubble tip,

$$\lim_{x\to\infty} h(x,t) = 1. \tag{2.6}$$

2.1. *Modelling assumptions*

Next, we describe several model assumptions which make the problem described above more manageable. We assume first that $\eta \gg 1$, so that the membrane tension greatly exceeds surface tension. As the bubble advances, a film of (typically) non-uniform thickness is deposited on the membrane behind the bubble tip. While the flux of fluid escaping past the bubble plays a significant role in the bubble dynamics, the subsequent surface-tension-driven redistribution of the film on the membrane is dynamically passive, since the membrane shape is controlled primarily by membrane tension rather than surface tension.

In the analysis below (§ 2.1.1–§ 2.1.2) it is convenient to split the flow domain into the four regions (I–IV) shown in figure 3. Approximate relationships for regions I, II and IV are derived below. The manner in which these are coupled to region III (which has fixed length and which contains the bubble tip) is discussed in detail in § 3.

2.1.1. *Modelling the flow around the bubble*

As shown in figure 3, the domain that spans the far-upstream region to the area directly downstream of the bubble tip comprises regions I–III. In regions I and II, the membrane and the adjacent fluid interface have small slope, since we assume $\eta \gg 1$. Thus the normal stress conditions (2.3*a*), (2.4*a*) reduce to

$$p - p_{\mathrm{b}} = f_{xx}, \quad p = \Gamma(h-1) - \eta h_{xx}. \tag{2.7}$$

Further, neglecting the contribution of surface tension to the membrane shape, (2.7) simplifies to

$$p_{\mathrm{b}} = \Gamma(h-1) - \eta h_{xx}. \tag{2.8}$$

Thus in regions I and II, the membrane has an equilibrium configuration, controlled at leading order by a balance of membrane tension and spring stiffness.

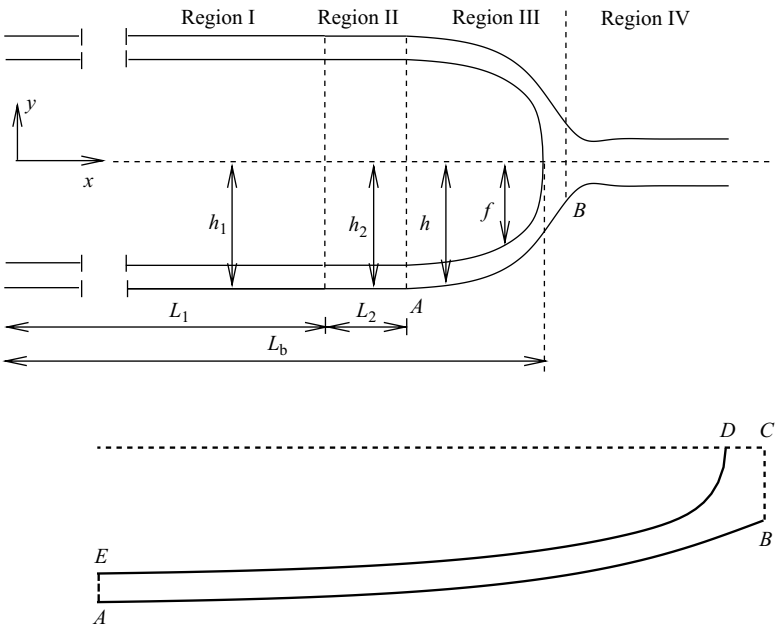

FIGURE 3. The flow domain (top) is split into four regions: region I is spatially uniform of length $L_1(t)$ where $L_{1t} = U$; region II is of fixed length L_2 where the membrane is in equilibrium but spatially non-uniform; region III is a fixed length region that includes the bubble tip; and region IV is the region ahead of the bubble. The boundary-element domain (below) consists of segments AB, BC, CD, DE and EA.

Far upstream is region I, which has length $L_1(t)$ that (by definition) grows at a rate equal to the bubble tip speed, so that $L_{1t} = U(t)$, $L_1(0) = 0$. Here the membrane is assumed to be spatially uniform, so that (from (2.8)) $h = h_1(t)$ where

$$h_1(t) \equiv (p_b/\Gamma) + 1. \tag{2.9}$$

Region II is of fixed length L_2 and it translates with the bubble tip. Here the membrane is spatially non-uniform but is again assumed to be in equilibrium, satisfying (2.8), so that

$$h(x,t) = [h_2(t) - h_1(t)]\,\frac{\sinh\,[\alpha(x - L_1(t))]}{\sinh(\alpha L_2)} + h_1(t) \qquad (L_1 < x < L_1 + L_2), \tag{2.10}$$

where $h_2(t) = h(L_1 + L_2, t)$ and $\alpha = \sqrt{\Gamma/\eta}$. In practice, $\alpha L_2 \gg 1$, so that the membrane asymptotes to h_1 within region II. $h_2(t)$ is determined by conditions in region III, as described in § 3 below.

2.1.2. *Modelling the flow ahead of the bubble*

Region IV lies far downstream of the bubble tip in the long fluid-filled channel where the membrane slope is uniformly small and thus lubrication theory is applicable. The liquid pressure here does not vary significantly across the film and is determined from (2.7*b*). The streamwise momentum equation (2.2*b*) reduces to $u_{yy} = p_x$, yielding

$$u = \tfrac{1}{2} p_x (y^2 - h^2). \tag{2.11}$$

Mass conservation then demands that

$$h_t + q_x = 0, \quad q = -\tfrac{1}{3}h^3 p_x, \quad p_x = \Gamma h_x - \eta h_{xxx}, \tag{2.12}$$

where q is the liquid flux in the laboratory frame.

2.1.3. *Pressure evolution equation*

We wish to simulate the system with either p_b or q_b prescribed. In the former case, we seek the evolution of f, h and U. In the latter case, an additional evolution equation for $p_\mathrm{b}(t)$ must to be derived. This equation arises from a macroscopic conservation of mass over regions I–III. The rate of change of bubble volume must equal the flow rate q_b, i.e.

$$q_\mathrm{b} = V_{\mathrm{I}t} + V_{\mathrm{II}t} + V_{\mathrm{III}t}, \tag{2.13}$$

where V_I, V_II and V_III are the bubble volumes in regions I, II and III, respectively:

$$V_\mathrm{I} = \int_0^{L_1(t)} f(x,t)\,\mathrm{d}x, \quad V_\mathrm{II} = \int_{L_1(t)}^{L_1(t)+L_2} f(x,t)\,\mathrm{d}x, \quad V_\mathrm{III} = \int_{L_1(t)+L_2}^{L_\mathrm{b}(t)} f(x,t)\,\mathrm{d}x. \tag{2.14}$$

In regions I and II the liquid is assumed to sit passively on the membrane wall. We differentiate $V_\mathrm{I} + V_\mathrm{II}$ with respect to time and apply the mass conservation condition

$$(h-f)_t + q_x = 0, \tag{2.15}$$

where $q = \int_f^h u\,\mathrm{d}y$ is the liquid flux in the laboratory frame. We assume $q(0,t) = 0$ and $q(L_1+L_2,t) = 0$, implying negligible surface-tension-driven flow of the liquid film. Then (2.9), (2.10) yield

$$V_{\mathrm{I}t} + V_{\mathrm{II}t} = \left[L_1 + L_2 - \frac{1}{\alpha}\left(\frac{c_\alpha - 1}{s_\alpha}\right)\right]\frac{p_{\mathrm{b}t}}{\Gamma} + \frac{1}{\alpha}\left(\frac{c_\alpha - 1}{s_\alpha}\right)h_{2t} - U\left(h_2 - \frac{p_\mathrm{b}}{\Gamma} - 1\right) + Uf(L_1+L_2,t),$$

where $c_\alpha \equiv \cosh(\alpha L_2)$, $s_\alpha \equiv \sinh(\alpha L_2)$ and $h_{2t} = Uh_x(L_1+L_2,t) + h_t(L_1+L_2,t)$. In addition, using (2.3*b*), $V_{\mathrm{III}t}$ can be expressed in terms of the surface velocity as

$$V_{\mathrm{III}t} = -Uf(L_1+L_2,t) - \int_0^{s_\mathrm{b}} \boldsymbol{u}|_{y=f}\cdot\boldsymbol{n}\,\mathrm{d}s, \tag{2.16}$$

where s is the arclength measured along the bubble surface from the bubble tip, and $s_\mathrm{b}(t)$ denotes the length of the bubble surface in region III. On applying (2.13), the evolution equation for the bubble pressure is obtained:

$$\frac{p_{\mathrm{b}t}L_1}{\Gamma} + \left\{\frac{p_{\mathrm{b}t}}{\Gamma}\left[L_2 - \frac{1}{\alpha}\left(\frac{c_\alpha-1}{s_\alpha}\right)\right] + \frac{h_{2t}}{\alpha}\left(\frac{c_\alpha-1}{s_\alpha}\right) - U\left(h_2 - \left(\frac{p_\mathrm{b}}{\Gamma}+1\right)\right)\right\} - \int_0^{s_\mathrm{b}} \boldsymbol{u}|_{y=f}\cdot\boldsymbol{n}\,\mathrm{d}s = q_\mathrm{b}(t). \tag{2.17}$$

The first term in (2.17) determines the rate of inflation or deflation of region I; the terms grouped in brackets $\{\cdots\}$ represent the rate of inflation or deflation of region II, and the integral arises from volume changes in region III. At steady state, (2.16) and (2.17) imply that $p_\mathrm{b} = \Gamma q_\mathrm{b}/U$ (noting that in this case $h - f = 1$ at $x = L_1 + L_2$).

Given an initial bubble shape and membrane wall deflection, values for the dimensionless spring stiffness Γ and wall tension η, and either a prescribed bubble pressure, p_b, or bubble flux, q_b, as defined in (2.1), the governing momentum and

continuity equations, (2.2), are solved numerically subject to the boundary conditions (2.3)–(2.6). The methods used to solve these equations are described next.

3. Methods of solution

Two approaches are used to solve this initial-value problem. The first (§ 3.1) involves the use of a two-dimensional boundary-element method (BEM), extending that presented in Gaver III *et al.* (1996) and Jensen *et al.* (2002) to incorporate unsteady effects. The second approach (§ 3.2) uses a one-dimensional asymptotic approximation, extending that presented in Jensen *et al.* (2002) and Naire & Jensen (2003). In both approaches the flow domain is divided into the four regions shown in figure 3, in which simplified approximate problems are solved as described in § 2.1: in regions I and II the membrane is assumed to be in equilibrium, to have small slope, and the deposited film is assumed dynamically passive; in region IV, (2.12) is used to model the interaction between the flow and the evolution of the membrane shape.

The primary difference between the BEM and asymptotic approaches is the treatment of region III. In the BEM approach, region III is a long computational domain that extends many channel widths upstream and downstream of the bubble tip (see domain A–E of figure 3). In this region, the full unsteady governing equations are solved subject to boundary conditions determined by patching to regions II and IV. Thus regions II–IV are simultaneously evolved as described in § 3.1 below. In the asymptotic approach, region III is centred on the bubble tip and is much shorter, with an order-unity aspect ratio; the membranes are assumed to be almost parallel and the local motion is assumed to be quasi-steady, allowing existing solutions of bubble flow in a weakly tapered channel to be exploited. Boundary conditions for the unsteady flow in region IV are determined by formal asymptotic matching.

3.1. *The boundary-element method (BEM)*

For given initial conditions (i.e. bubble and membrane shapes and q_b or p_b) we compute the unknown velocity or stress fields on the boundaries of region III by integrating numerically the boundary-element equations. We march in time by solving the kinematic boundary conditions on the bubble and membrane interfaces, which are coupled to regions II and IV as described below.

Stokes' equations (2.2), at any given time t, are solved by using Green's theorem to derive an integral equation involving the velocity and stress on the boundary S of region III,

$$C_{ki}u_i(\boldsymbol{x}) + \int_S T_{ik}(\boldsymbol{x}, \boldsymbol{y})u_i(\boldsymbol{y})\,\mathrm{d}s(\boldsymbol{y}) = \int_S U_{ik}(\boldsymbol{x}, \boldsymbol{y})\tau_i(\boldsymbol{y})\,\mathrm{d}s(\boldsymbol{y}), \tag{3.1}$$

where $\boldsymbol{x}$ represents the position vector of a point on S, C_{ki} is a matrix which allows for a jump in normal stress, and $\boldsymbol{\tau} = \boldsymbol{\sigma}\cdot\boldsymbol{n}$ is the stress vector, $\boldsymbol{n}$ being the unit outward normal to S. The kernels U_{ik} and T_{ik} are

$$U_{ik}(\boldsymbol{x}, \boldsymbol{y}) = -\frac{1}{4\pi}\left(\delta_{ik}\log|\boldsymbol{x}-\boldsymbol{y}| - \frac{(x_i-y_i)(x_k-y_k)}{|\boldsymbol{x}-\boldsymbol{y}|^2}\right), \tag{3.2a}$$

$$T_{ik}(\boldsymbol{x}, \boldsymbol{y}) = -\frac{1}{\pi}\frac{(x_i-y_i)(x_j-y_j)(x_k-y_k)n_j(\boldsymbol{y})}{|\boldsymbol{x}-\boldsymbol{y}|^4}. \tag{3.2b}$$

To solve (3.1), S is discretized into N elements, each consisting of 3 node points. The position, velocity and stress fields are approximated using quadratic polynomials

over each element. A linear system of equations is then obtained for the unknown velocities and stresses on each of the boundaries

$$H\boldsymbol{w} = G\boldsymbol{t}, \tag{3.3}$$

where H and G are respectively $4N \times 4N$ and $6N \times 6N$ matrices whose entries are computed using Gaussian quadrature rules, and $\boldsymbol{w}$ and $\boldsymbol{t}$ are vectors of velocities and stresses at each of the N nodes. Applying the boundary conditions (see below), (3.3) can be rearranged into a system of equations for the unknown velocities and stresses which is solved using Gaussian elimination with partial pivoting.

The boundary S is divided into five piecewise smooth segments (A–E in figure 3) along which either velocity or stress conditions are applied. Given an initial bubble shape, its curvature can be computed, and hence the normal stress condition (2.3a) is known along segment DE. Along segment AB, the horizontal component of velocity is zero and the vertical component of the stress condition is prescribed by (2.4a). Along segment CD, the symmetry conditions (2.5) are applied. Along segment EA, we impose $u = 0$ (in the laboratory frame) and $\tau_y = 0$. Along segment BC, we specify a horizontal component of velocity given by (2.11) and a vertical shear stress component τ_y which is obtained by differentiating (2.11), which couples the flow to region IV. At the corner B, we require that the position, slope and curvature of the membrane be continuous.

Time-stepping for the evolution of regions I–IV occurs using an implicit time-stepping method (LSODES, see Hindmarsh 1982). The evolution for region III is simulated by solving (2.3b) and (2.4c) using velocities from the BEM solution. Simultaneously, the membrane shape in region IV is determined by solving (2.12) using the method of lines with the spatial derivatives approximated using finite differences over a non-uniform grid. Region II adapts itself automatically to the evolution of region III following (2.10). Simultaneous time-stepping of regions II–IV is essential to provide the necessary end conditions for region III. The bubble tip velocity is subtracted from the x-component of velocity in the kinematic boundary conditions, which allows our domain to be fixed to the bubble-tip frame of reference. After solving the membrane and meniscus shapes, the flow field can be readily computed.

A different approach is taken when seeking steady-state solutions. In this case an iterative scheme using Newton's method on the kinematic boundary conditions is used to update the shapes of the meniscus and the membrane. This method improves upon the technique described in Gaver III *et al.* (1996) by simultaneously iterating both the meniscus and membrane shapes.

3.2. *Asymptotic reopening model*

The formal aspects of the asymptotic model under steady conditions are discussed in Jensen *et al.* (2002). Here, we briefly present the analogous unsteady version, following Naire & Jensen (2003) who treated a different initial-value problem in a related physical system. We develop an asymptotic expansion in the small parameter $\epsilon = \eta^{-1/3} \ll 1$, assuming that the membrane slope is uniformly small. Once again, in regions I and II the membrane is in equilibrium and the deposited film plays no dynamical role. In region III, now assumed to have $O(1)$ length and width, the local Stokes flow around the bubble tip is two-dimensional and is assumed to be quasi-steady (relative to the slow evolution of region IV). Since the membrane slope is small, the flow here is equivalent to that of a bubble in a weakly tapered channel. We exploit previous numerical studies of this problem (Halpern & Jensen 2002) to provide estimates of key flow quantities (the pressure drop across the bubble tip, and

the thickness of the deposited film) that we incorporate into boundary conditions for region IV; this region is described using lubrication theory.

We move to the bubble tip frame and make a long-wavelength approximation by setting

$$X = \epsilon(x - L_b(t)), \quad T = \epsilon t, \quad H(X,T) = h(x,t), \quad P = \epsilon p, \quad P_b = (\epsilon/\delta)p_b, \tag{3.4}$$

where the parameter $\delta = \sqrt{\epsilon\Gamma}$ is assumed to be $O(1)$. Then, in region IV, (2.12) becomes

$$H_T + Q_X = 0, \quad Q = -\tfrac{1}{3}H^3 P_X - HU, \quad P = \delta^2(H-1) - H_{XX}, \tag{3.5}$$

in $X \geqslant 0$, where Q is the two-dimensional volume flux in the frame of the bubble tip. Equations (3.5*a–c*) are solved subject to boundary conditions obtained by matching to regions I and II. To explain these, we first re-write (2.10) using (3.4), assuming $\alpha L_2 \gg 1$, so that in region II

$$H = (h_2 - h_1)\,\mathrm{e}^{\delta(X+\epsilon L_3)} + h_1, \quad h_1 = (P_b/\delta) + 1, \quad L_3 = L_b - L_1 - L_2 = O(1),$$

and deduce that

$$H_X(0) = \delta(h(0) - 1) - P_b + O(\epsilon^2), \qquad H_{XX}(0) = \delta^2(h(0) - 1) - \delta P_b + O(\epsilon^2). \tag{3.6}$$

The boundary conditions we apply to (3.5) are then

$$H_X(0,T) = -\theta = -P_b(T) + \delta(H_b - 1), \tag{3.7a}$$

$$H_{XX}(0,T) = \delta^2(H_b - 1) - \delta P_b - \epsilon U \mathscr{P}_0(U)/H_b, \tag{3.7b}$$

$$Q(0,T) = -\lambda(U, \epsilon\theta)H_b U, \tag{3.7c}$$

$$\lim_{X\to\infty} H(X,T) = 1. \tag{3.7d}$$

Here $H_b(T) = H(0,T)$ is the membrane width at the bubble tip. Equation (3.6*a*) shows that (3.7*a*) ensures continuity of slope across region III; (3.6*b*) shows that (3.7*b*) is a pressure balance, supplemented with a term $\mathscr{P}_0(U)$ representing the pressure jump across the tip of a semi-infinite bubble in a parallel-sided channel at capillary number U. Equation (3.7*c*) is a flux balance; here $\lambda(U, \epsilon\theta) = \lambda_0(U) + \epsilon\theta\lambda_1(U)$ is the film thickness left behind a meniscus advancing with speed U through a uniformly tapered channel with taper angle $\epsilon\theta \ll 1$. We use regression formulae for λ_0, λ_1 and $\mathscr{P}_0$ given in Jensen *et al.* (2002), obtained from a range of numerical studies (and repeated for convenience in Appendix A). Equations (3.5)–(3.7) have error $O(\epsilon^2)$ as $\epsilon \to 0$ with $\delta = O(1)$.

The relationship between the rate of change of pressure and the flow rate (2.17) after scaling (using (3.4)) is

$$Q(0,T) = q_b - \frac{P_{bT}}{\delta}\left(\mathscr{L} - \frac{1}{\delta}\right) - U\left(1 + \frac{P_b}{\delta}\right) - \frac{H_{bT}}{\delta}(1 - \delta\epsilon L_3), \tag{3.8}$$

where $\mathscr{L} = \epsilon L_b$ and L_3 is the $O(1)$ length of region III. In the following L_3 was set to zero; this made negligible difference to the results.

3.3. *Validation of steady solutions*

We tested the present reopening models against that of Gaver III *et al.* (1996) by computing steady solutions with $\Gamma = 0.5$, $\eta = 100$. The models presented herein have slightly different wall boundary conditions from those of Gaver III *et al.* (1996) as discussed in § 2.1. Specifically, instead of (2.4*b*, *c*), Gaver III *et al.* (1996) used the

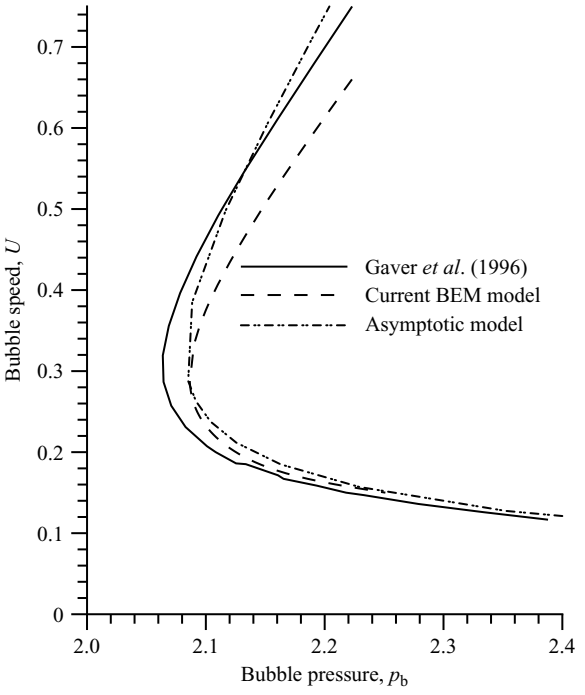

FIGURE 4. Bubble speed U versus bubble pressure p_b for steadily propagating bubbles, showing comparisons between current BEM model (dashed), the asymptotic model (dot-dashed) and previous results of Gaver III *et al.* (1996) (solid), for $\eta = 100$, $\Gamma = 0.5$.

following kinematic boundary conditions at the membrane in a bubble-tip frame of reference:

$$u = n_x^2 - 1, \; v = n_x n_y, \tag{3.9}$$

corresponding to a travelling wave propagating at the same speed as the meniscus tip, which is only appropriate for steady state motion. If a small-slope approximation is made, in steady state these conditions are identical to (2.4*b*, *c*) (noting that the latter are given in the laboratory frame). Also, Gaver III *et al.* (1996) applied a stress boundary condition normal to the wall, while in (2.4*a*) we apply the condition in the vertical direction only. As with the kinematic boundary conditions (2.4*b*, *c*), these are equivalent in the small-slope limit. These modifications of the boundary conditions provide only slight differences in the solutions, as we shall see below.

Figure 4 shows the pressure–speed relationship for steadily propagating bubbles. The figure demonstrates that the agreement between BEM computations, the asymptotic model and predictions from Gaver III *et al.* (1996) is very good for small U, but small deviations occur as U increases. The closeness of the results at small U (for 'pushing' solutions) may be attributed to the fact that the wall slope is small over most of the wall and therefore $n_x \approx 0$ in (3.9); this results in $u \approx 0$, exactly the boundary condition used in the current model (see 2.4*b*). The deviation between the asymptotic model and numerical results of Gaver III *et al.* (1996) increases slightly as U increases along the 'peeling' solution branch because the small-slope assumption is less accurate.

4. Numerical results

In this section we examine the stability of the steady solutions found in § 3.3 (figure 4) using the time-dependent models derived above. We examine perturbations both in bubble pressure (§ 4.1) and volume flux (§ 4.2) to representative pushing and peeling solutions (indicated with symbols in figure 2), each of which has $p_b = 2.23$ (according to BEM) at steady state.

4.1. *Stability of pressure-driven reopening*

To examine the stability of the two branches of the steady solution curve shown in figure 4, p_b was perturbed according to

$$p_b(t) = \begin{cases} p_{b0} + \frac{1}{2}\Delta p_b(1 - \cos(2\pi t/\Delta t)), & 0 \leqslant t \leqslant \Delta t, \\ p_{b0}, & t > \Delta t, \end{cases} \tag{4.1}$$

where p_{b0} is the initial pressure, and $|\Delta p_b|$ is the maximum bubble pressure perturbation, occurring at $t = \Delta t/2$.

4.1.1. *Stability of peeling motion*

The response of the peeling solution at $p_{b0} = 2.23$ to a positive pressure perturbation is shown in figure 5. Both the BEM and asymptotic models show the bubble speed returning to its initial value for $t > \Delta t$. Note that the discrepancy between the solutions provided by the two approaches is similar in magnitude to that demonstrated in figure 4. Similar behaviour was observed for a negative pressure perturbation (not shown). In all cases that we examined, steady peeling solutions were found to be stable to finite pressure disturbances for which p_b returns to its original value.

4.1.2. *Stability of pushing motion*

Figure 6 illustrates the response of the pushing solution at $p_{b0} = 2.23$ to a positive pressure perturbation acting over 300 time units (figure 6*a*). The tip velocity initially increases quite slowly, then accelerates at $t = 15000$ and eventually approaches the steady peeling velocity having the same value of p_{b0} (figure 6*b*). Again, the BEM and asymptotic methods both predict very similar behaviour. This validates our simulation methods and justifies the assumption (for the one-dimensional simulations) that the flow near the bubble tip is quasi-steady. Figure 6(*c*) shows how, as U increases towards its steady peeling value for $t > \Delta t$, the bubble tip becomes more pointed and the membrane develops a characteristic damped wavy shape. Correspondingly, the vertical component of stress along the wall, τ_y, develops a deep minimum coincident with the region of high membrane curvature, characteristic of peeling motion (figure 6*d*).

In contrast, if the same pushing solution ($p_{b0} = 2.23$) is subject to a negative pressure perturbation (figure 7*a*), the tip velocity initially decreases and increases in concert with the fall and rise of p_b. However, after the pressure perturbation is complete the velocity overshoots its initial value slightly and then falls indefinitely (figure 7*b*). As the bubble slows, the thickness of the film being deposited behind the tip decreases, and fluid accumulates ahead of the bubble tip, as shown in figure 7(*c*). The vertical component of stress decreases more gently towards zero as the length of the filling region increases (figure 7*d*).

A transition from peeling to similar unsteady pushing behaviour can be obtained if a peeling solution is subject to a sustained reduction in bubble pressure, so that p_b is reduced to $p_b < p_{crit}$. The large-time behaviour then resembles that shown in figure 7. The bubble acts as a leaky piston, continually accumulating fluid ahead of the tip, but slowing as the lengthening fluid column is displaced under a fixed pressure drop.

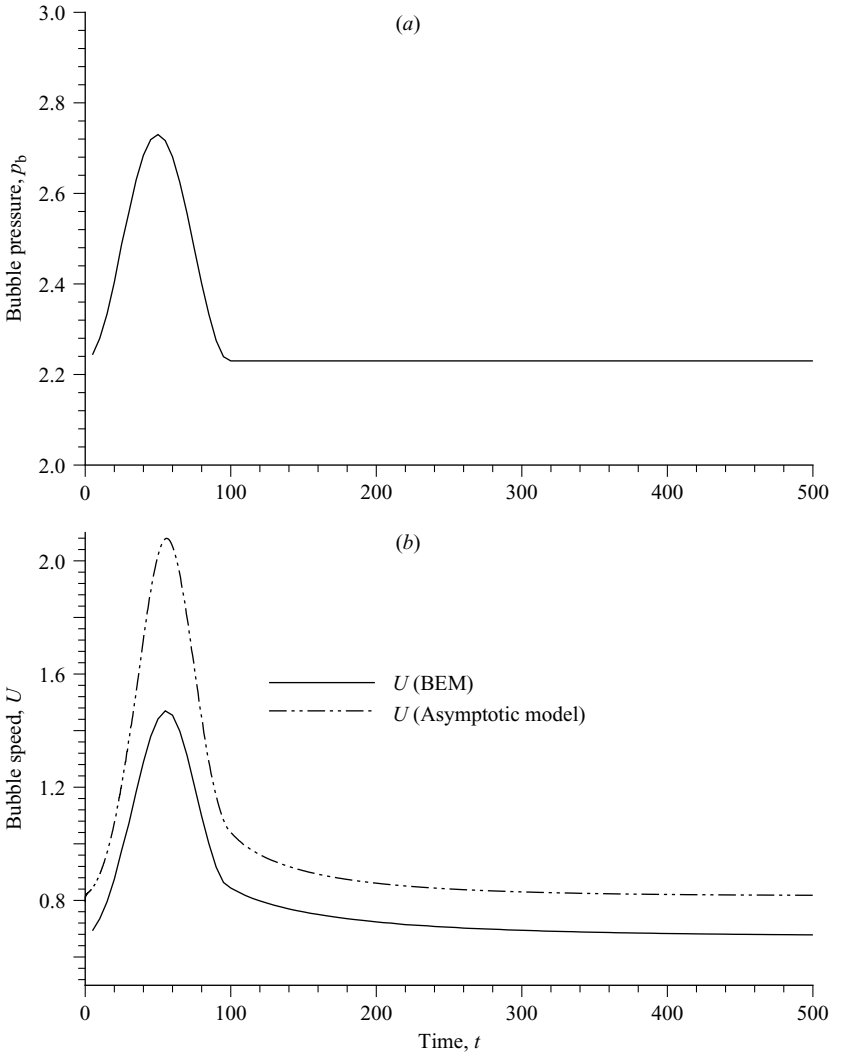

FIGURE 5. The effect of a positive pressure perturbation (a) (with $\Delta p_b = 0.5$, $\Delta t = 100$ in (4.1)) on the tip velocity (b) of a peeling solution, with $\Gamma = 0.5$, $\eta = 100$, $p_{b0} = 2.23$.

This behaviour is analysed further in § 5 below, where the self-similar nature of the large-time evolution in figure 7 is described, and the dynamics of unsteady pushing motion is characterized using a simple first-order ODE.

4.2. *Stability of flow-driven reopening*

We now examine the stability of the same steady solutions to perturbations in q_b, given by

$$q_b(t) = \begin{cases} q_{b0} + \frac{1}{2}\Delta q_b(1 - \cos(2\pi t/\Delta t)), & 0 \leqslant t \leqslant \Delta t, \\ q_{b0}, & t > \Delta t, \end{cases} \tag{4.2}$$

where q_{b0} is the initial (steady) flow rate, and $|\Delta q_b|$ is the maximum flux perturbation occurring at $t = \Delta t/2$.

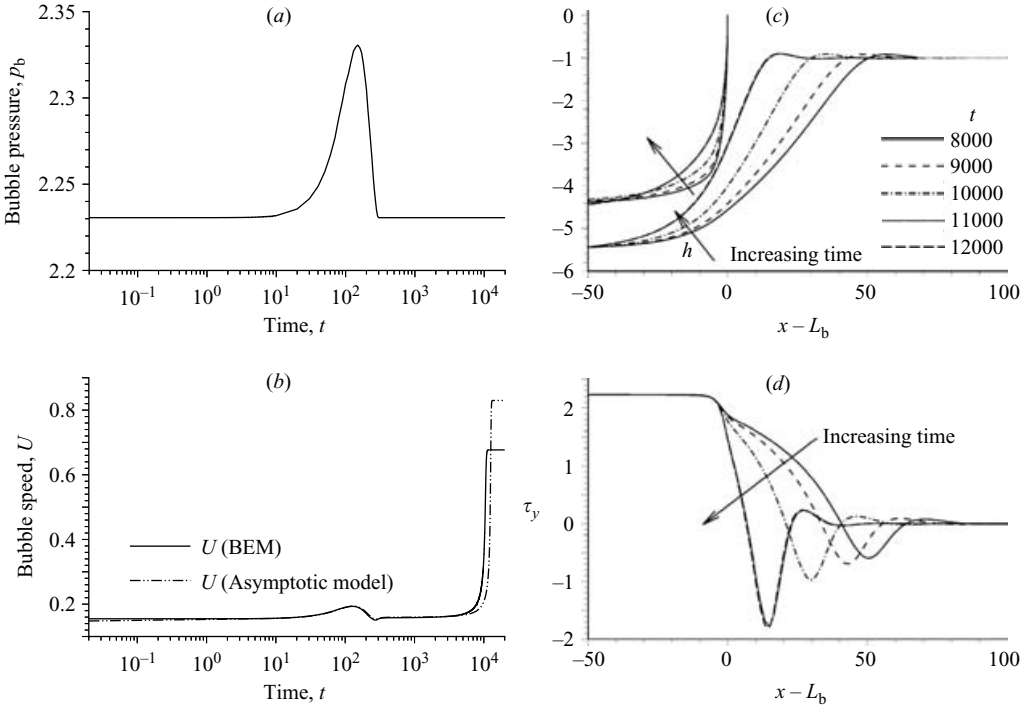

FIGURE 6. The effect of a positive pressure perturbation ($\Delta p = 0.1$, $\Delta t = 300$) on the steady pushing solution with $p_{b0} = 2.23$, showing evolution towards steady peeling; other parameter values as for figure 5. (*a*) p_b and (*b*) U versus t; (*c*) membrane and bubble shapes and (*d*) vertical stress versus $x - L_b$, at $t = 8000$, 9000, 10000, 11000 and 12000, obtained using BEM calculations.

4.2.1. *Stability of peeling motion*

Figure 8 demonstrates how the steady peeling solution with $q_{b0} = 3$ (and $p_b = 2.23$ based on BEM) is stable to a large positive flow-rate perturbation. Both U and p_b increase as q_b increases with time (figure 8*a*, *b*). We define the parameter $q_b\Gamma/(Up_b)$, as an 'unsteadiness' parameter. Since p_b/Γ is the bubble width, $q_b\Gamma/(Up_b) = 1$ if the flow is steady. Figure 8 shows that the unsteadiness parameter initially rises above unity, but begins to decrease before q_b reaches its maximum (figure 8*c*). In contrast, p_b and U continue to rise until after q_b begins to decline. At some point $q_b\Gamma/Up_b < 1$, but it eventually increases towards unity, as both p_b and U decrease towards their steady-state values, exhibiting a weak overshoot in doing so. Very similar behaviour was seen when a negative perturbation ($\Delta q_b = -1$) was applied (not shown). Once again, solutions obtained using the BEM and asymptotic models show qualitatively similar behaviour.

4.2.2. *Stability of pushing motion*

The evolution of a steady pushing solution to either positive or negative perturbations of q_b is shown in figure 9. Here $\Delta q_b = 0.31$ and -0.29, $\Delta t = 500$, $L_b(0) - L_2 = 50$ and only BEM simulations are shown. During the perturbation, U and p_b vary smoothly and appear, initially, to settle back to their original values, albeit with a slight overshoot that is not evident in the figure. However over very long times, U and p_b exhibit unexpected non-periodic oscillations (figure 9*a*, *b*). This type of oscillation

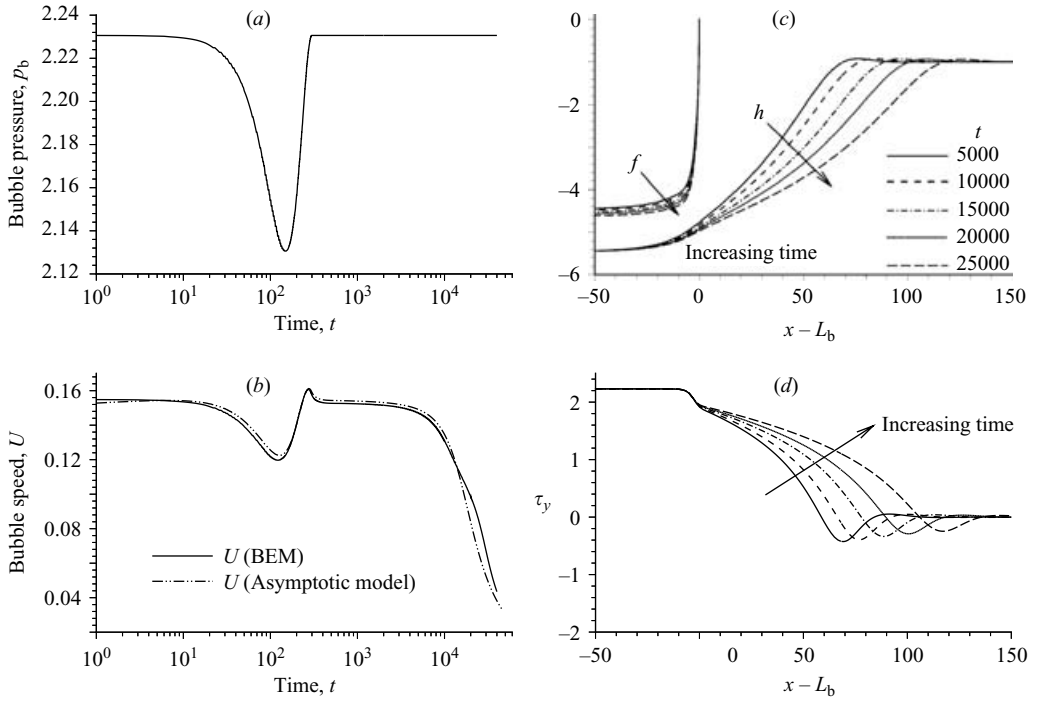

FIGURE 7. The effect of a negative pressure perturbation ($\Delta p = 0.1$, $\Delta t = 300$) on the steady pushing solution with $p_{b0} = 2.23$, showing the transition to continually slowing unsteady pushing; other parameter values as for figure 5. (*a*) p_b and (*b*) U versus t; (*c*) membrane and bubble shapes and (*d*) vertical stress versus $x - L_b$, at $t = 5000$, 10000, 15000, 20000 and 25000, obtained using BEM calculations.

also arises if $\Delta q_b = 0$. In this case the perturbation arises due to very slight 'noise' that inevitably appears in numerical simulations.

Figure 9 demonstrates that the oscillations have very long periods, and show a dramatic increase in amplitude as t increases. The phase but not the character of the instability is sensitive to the sign of the initial perturbation in Δq_b. During each oscillation, the bubble propagates very slowly for long periods of time as p_b rises gently; then, suddenly, U rises dramatically, and then both U and p_b fall to low values once more. The growing oscillations are conveniently plotted on the (p_b, U)-phase plane (figure 9*c*), which highlights the two phases in each oscillation. First the bubble progresses for long periods of time in an unsteady pushing mode (below the steady pushing curve). During this stage the channel slowly inflates while U decreases slowly and p_b increases slowly. Then U begins to increase, first slowly and then very rapidly while p_b remains nearly constant. At this point the pushing behaviour quickly switches to quasi-steady peeling motion as a large amount of fluid is able to escape past the bubble tip. However once in the peeling mode, q_b is too small to sustain high-speed motion, and the solution drifts down the steady peeling branch (with U and p_b both decreasing) to the minimum of the steady solution curve. The cycle then repeats, but with a bubble that is much longer than during the prior oscillation. This causes the following pressure and velocity excursions to be much greater. The essential elements of the dynamics of this oscillation are captured using a third-order ODE model in § 5 below.

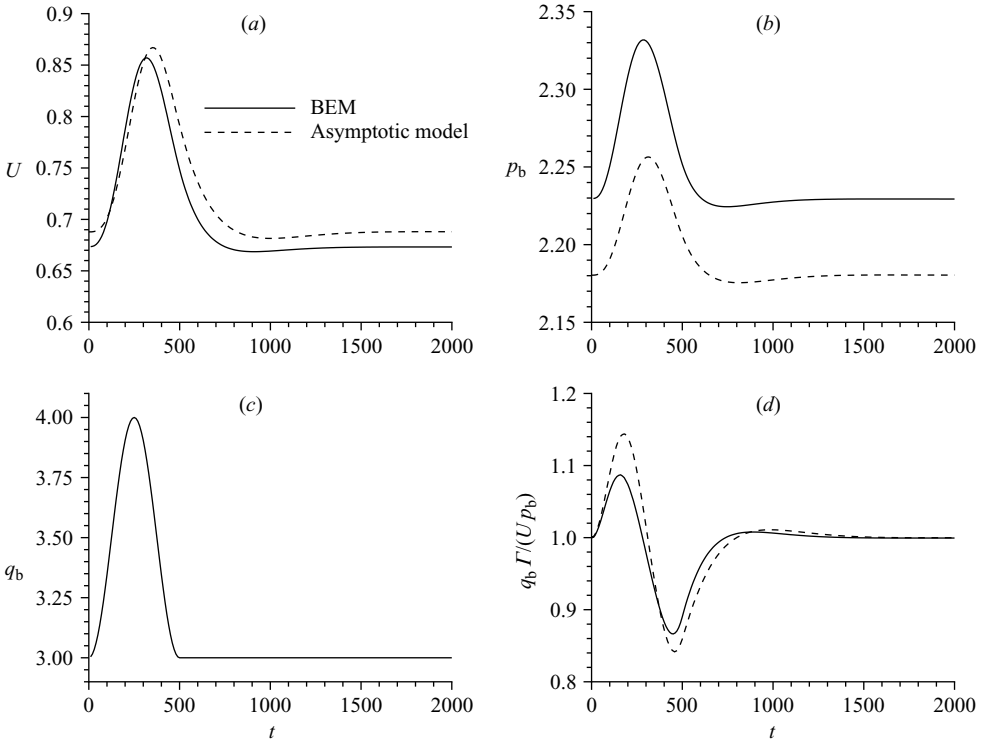

FIGURE 8. The effect of a positive flow-rate perturbation ($\Delta q_b = 1$, $\Delta t = 500$) on the peeling steady solution for which $q_{b0} = 3$, $\Gamma = 0.5$ $\eta = 100$, computed using BEM (solid) and the asymptotic model (dashed). (*a*) U versus t; (*b*) p_b versus t; (*c*) q_b versus t; (*d*) $q_b\Gamma/(Up_b)$ versus t.

To validate the BEM predictions, simulations using both BEM and the asymptotic model are presented in figure 10, for which the flow rate is ramped down from $q_b = 3$ to 1 and then held constant (figure 10*c*). Solutions obtained independently with the two solution methods show good qualitative agreement, even when integrated over long times. However, the asymptotic model has the advantage that long-time integrations are considerably less expensive than with BEM. Once again, since the bubble is elongating the system is continually changing size, and the period and amplitude of oscillations both increase as the bubble lengthens.

In summary, with q_b prescribed, the simulations we conducted all suggest that the peeling branch (i.e. for $q_b > q_{crit}$ where q_{crit} is the flux corresponding to the turning point of the p_b–U curve, see figure 2) is stable to either a positive or negative perturbation of q_b. Such a perturbation causes the system to overshoot in an oscillatory fashion, followed by a decay to the corresponding steady state on the peeling branch. For the pushing branch ($q_b < q_{crit}$), however, we find that the corresponding steady solution appears stable for intermediate times but eventually loses stability as the bubble grows in length (figures 9 and 10). We have isolated the cause of the instability as the term $p_{bt}L_1$ in (2.17), which contributes to changes in the bubble volume via transverse inflation. Since the magnitude of the volume variation is proportional to L_1, this term becomes significant only when L_1 is large (i.e. when the bubble is sufficiently long). This allows small fluctuations in p_b to induce

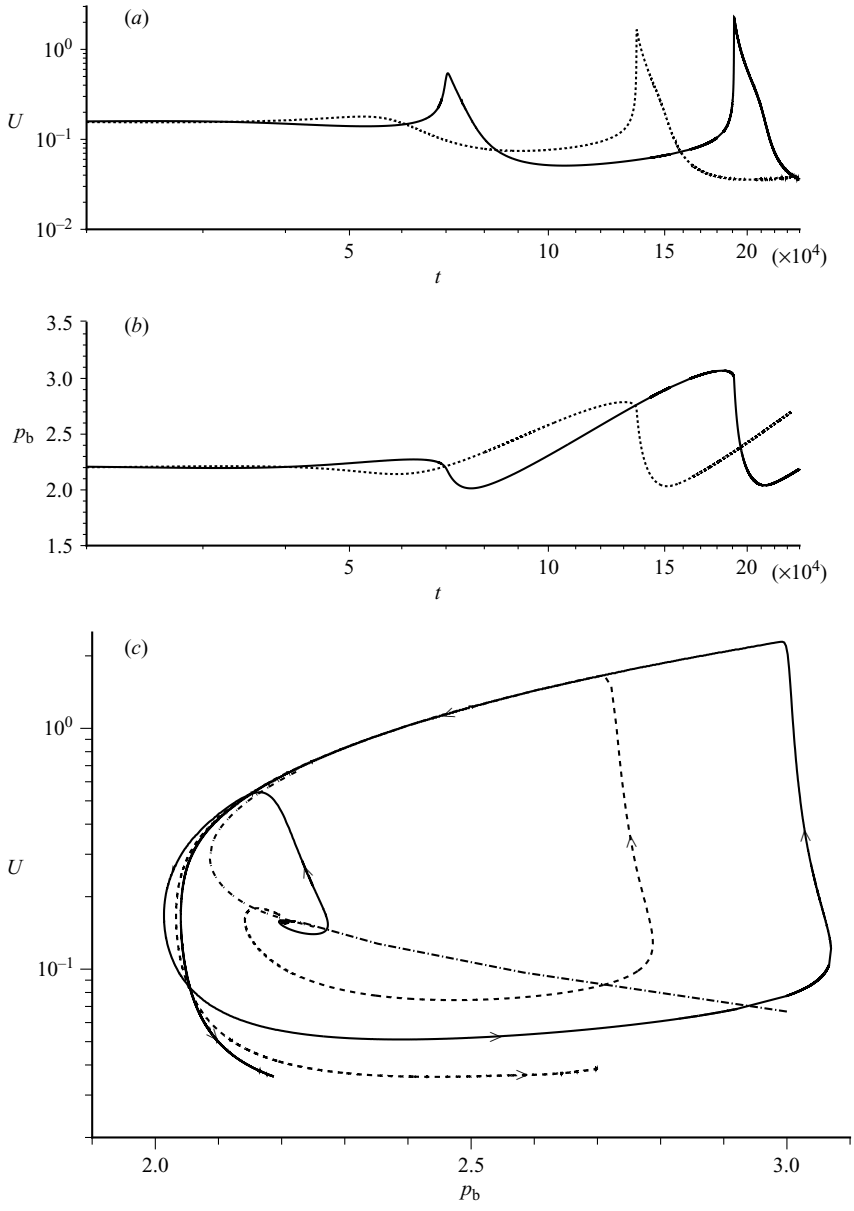

FIGURE 9. An example of the system exhibiting growing non-periodic, large-amplitude relaxation oscillations for $t > 2000$. (*a*) Tip velocity U versus t; (*b*) bubble pressure p_b versus t; and (*c*) U versus p_b, where arrows indicate increasing time. Here $q_b = 1.25$, $\Gamma = 0.5$, $\Delta t = 500$ and $L_2 = 80$. The solid lines correspond to a positive pressure perturbation $\Delta q_b = 0.31$, and the dashed lines to a negative pressure perturbation (to a steady pushing solution) with $\Delta q_b = -0.29$. Also shown in (*c*) are the steady-state solutions (the dash-dot line) consisting of solutions obtained from BEM for $U > 0.15$ and from the asymptotic model for $U < 0.15$.

large changes in bubble volume. Switching off this term in simulations suppresses the instability and stabilizes pushing solutions. The mechanism underlying the instability is explored further below.

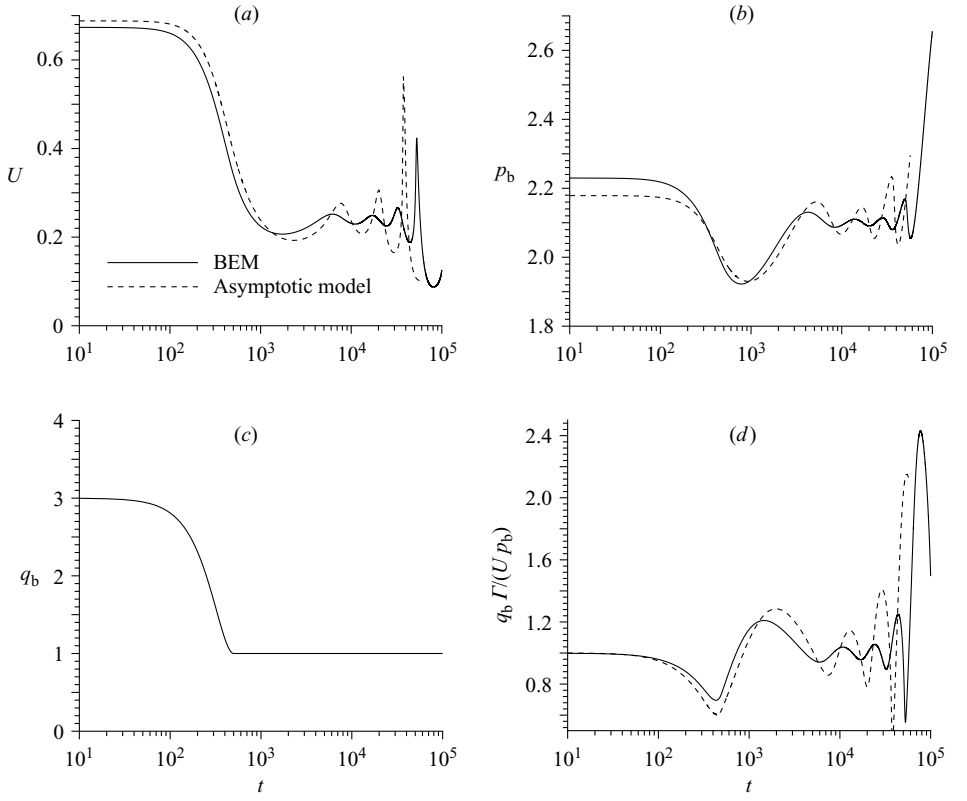

FIGURE 10. The effect of a reduction in flow rate from $q_b = 3$ to $q_b = 1$. (*a*) U versus t; (*b*) p_b versus t; (*c*) q_b versus t; (*d*) $q_b\Gamma/(Up_b)$ versus t.

5. A lumped-parameter model of unsteady pushing and peeling

We have demonstrated that a bubble propagating into a flexible channel can exhibit either an ever-slowing pushing motion at low speeds when $p_b(< p_{crit})$ is prescribed or alternating pushing/peeling motion when $q_b(< q_{crit})$ is prescribed. To gain further insight into these instabilities, we now characterize unsteady pushing and quasi-steady peeling motion with a simple lumped-parameter model that highlights the key physical mechanisms operating in each case.

5.1. *Unsteady pushing*

A channel being inflated in the pushing mode is sketched in figure 11. This mode can be characterized by a long expanded region that extends ahead of the bubble tip of approximate length $\mathscr{L}(t)$ and volume per unit width $\mathscr{V}(t)$. We may represent the bubble with its height $\mathscr{W}(t)$, length $L_b(t)$ and tip speed $U(t) = L_{bt} \ll 1$. In what follows we aim to capture only basic scaling relationships between these variables rather than to be quantitatively accurate, and so most numerical coefficients are set to unity.

Conservation of fluid volume in the region surrounding the bubble tip gives

$$\mathscr{V}_t = U(1 - \lambda(U)\mathscr{W}) \tag{5.1}$$

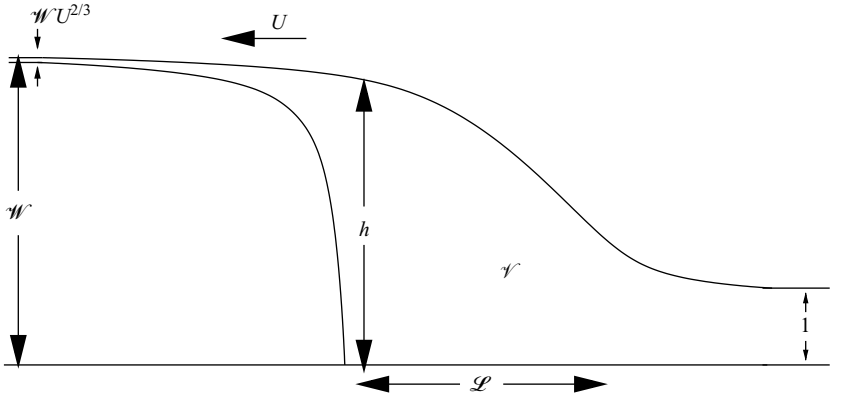

FIGURE 11. Schematic of unsteady pushing motion.

using the quasi-steady flux condition (3.7*c*), where λ is the film-thickness function discussed in § 3.2 (see also Appendix A); at low speeds $\lambda \sim U^{2/3}$ (Bretherton (1961)), which is appropriate in the pushing regime.

Two methods can be used to estimate $\mathscr{L}$. Balancing the two terms that contribute to the volume flux within $\mathscr{V}$ (see (2.12*b*)) provides $h^3 p_x \sim Uh$. Integrating this relationship over x while assuming h is nearly constant over the length $\mathscr{L}$, and noting that the pressure scales as $p_\mathrm{b} \sim \Gamma h$ (see (2.7*b*)), we estimate $\mathscr{L} \sim \Gamma h^3/U$ where $h \sim \mathscr{W}$. Alternatively, the estimate of $\mathscr{L}$ follows from the integral force balance

$$p_\mathrm{b}\mathscr{W} = \int_0^{\mathscr{L}} \tau \, \mathrm{d}x \tag{5.2}$$

where τ is the horizontal component of stress along the wall downstream of the bubble tip. Equation (2.11) implies $\tau \sim p_x h$; the quasi-steady flux balance (2.12*b*) implies $\tau \sim U/h$, so that (5.2) becomes $p_\mathrm{b}\mathscr{W} \sim U\mathscr{L}/\mathscr{W}$, and hence $\mathscr{L} \sim p_\mathrm{b}^3/(\Gamma^2 U)$, given that $\mathscr{W} \sim p_\mathrm{b}/\Gamma$ (from (2.8)).

The volume $\mathscr{V} \sim \mathscr{W}\mathscr{L}$ can then be estimated to be

$$\mathscr{V} \sim \Gamma \mathscr{W}^4/U \sim p_\mathrm{b}^4/\Gamma^3 U, \tag{5.3}$$

given that $\mathscr{W} \gg 1$. Assuming p_b (and hence $\mathscr{W}$) is held fixed, (5.1) reduces (modulo $O(1)$ numerical factors) to

$$U_t = -\frac{U^3\Gamma^3}{p_\mathrm{b}^4}\left(1 - \frac{p_\mathrm{b}U^{2/3}}{\Gamma}\right). \tag{5.4}$$

Equation (5.4) provides a closed system parameterized by p_b and Γ. Its dynamics are described in § 5.3 below. It is a statement of conservation of liquid volume ahead of the bubble, incorporating an expression relating the pressure drop across the liquid volume to viscous resistance as it advances.

If instead q_b is prescribed, since the bubble volume $V_\mathrm{b} \approx \mathscr{W} L_\mathrm{b}$, the flux $q_\mathrm{b} = V_{\mathrm{b}t}$ satisfies

$$q_\mathrm{b} = (p_\mathrm{b}U + p_{\mathrm{b}t}L_\mathrm{b})/\Gamma. \tag{5.5}$$

Using (5.3*b*) and (5.5), (5.1) can be written as

$$U_t = \frac{4U}{p_\mathrm{b}L_\mathrm{b}}(\Gamma q_\mathrm{b} - p_\mathrm{b}U) - \frac{\Gamma^3U^3}{p_\mathrm{b}^4}\left(1 - \frac{p_\mathrm{b}}{\Gamma}U^{2/3}\right), \tag{5.6a}$$

which, along with

$$L_{bt} = U, \tag{5.6b}$$

$$p_{bt} = (\Gamma q_b - p_b U)/L_b, \tag{5.6c}$$

provides a closed system, parameterized by q_b and Γ. Note that if p_b is held fixed, $q_b = p_b U/\Gamma$ and (5.6*a*) reduces to (5.4). Equation (5.6*a*) again expresses conservation of liquid volume, but it additionally accounts for volume changes arising from temporal variations in p_b driven by inflation of the bubble. As we show in § 5.4 below, it accounts for the unsteady pushing phase of an oscillation; to capture a complete oscillation, we must also describe peeling.

5.2. *Quasi-steady peeling*

In the same spirit as § 5.1, we assume that the steady peeling branch lies along $p_b = \Gamma^{1/2}\eta^{1/6}U^{1/3}$, consistent with the asymptotic limit identified in Jensen *et al.* (2002). As before, the pushing branch is taken to lie along $p_b = \Gamma U^{-2/3}$. These are approximations to the two solution branches in figure 2(*a*). The pushing and peeling branches are assumed to terminate at their intersection point $(p_c, U_c) = (\Gamma^{2/3}\eta^{1/9}, \Gamma^{1/2}\eta^{-1/6})$ (a crude estimate of the true turning point (p_{crit}, U_{crit})). When $q_b < p_c U_c/\Gamma$ is held fixed, we would like to be able to describe how during an oscillation the solution tracks quasi-steadily down the peeling branch from some initial state (p_m, U_m), where $U_m = p_m^3\Gamma^{-3/2}\eta^{-1/2}$, to (p_c, U_c).

From (2.8), the bubble volume $V_b \approx (1 + (p_b/\Gamma))(L_b - \sqrt{\eta/\Gamma})$. Assuming that $1 \ll \eta \ll L_b^2$, we may write $V_b \approx p_b L_b/\Gamma$. The motion of the bubble then satisfies $q_b = V_{bt}$ and $U = L_{bt}$. Treating L_b as an independent variable, we therefore have

$$q_b = U\frac{\mathrm{d}}{\mathrm{d}L_b}\left(\Gamma^{-1/2}\eta^{1/6}U^{1/3}L_b\right). \tag{5.7}$$

Integrating (5.7) and imposing the initial condition $U = U_m$ when $L_b = L_m$, say, we may therefore describe quasi-steady peeling using

$$q_b\left(L_b^4 - L_m^4\right) = \eta^{1/6}\Gamma^{-1/2}\left(L_b^4 U^{4/3} - L_m^4 U_m^{4/3}\right), \quad U = L_{bt}. \tag{5.8}$$

Assuming $L_b = L_c$ when U falls to U_c, (5.8) becomes

$$\frac{L_c}{L_m} = \left(\frac{p_m U_m/\Gamma - q_b}{p_c U_c/\Gamma - q_b}\right)^{1/4}. \tag{5.9}$$

This equation describes the proportional growth in bubble length during peeling as U decreases from U_m to U_c.

Combining (5.6) to describe pushing and (5.8) to describe peeling, we are now in a position to reproduce a full nonlinear relaxation oscillation with prescribed q_b. First, however, we consider behaviour with fixed p_b.

5.3. *Unsteady motion at fixed* p_b

Equation (5.4) provides a model equation capturing unsteady pushing motion at fixed p_b. The fixed point, $p_b = \Gamma U^{-2/3}$, approximating the steady pushing branch of solutions when $U \ll 1$, is evidently unstable according to (5.4). If $p_b < \Gamma U^{-2/3}$, $U_t < 0$ and thus U diminishes indefinitely. Furthermore, (5.4) predicts that $U \propto t^{-1/2}$as $t \to \infty$. If $p_b > \Gamma U^{-2/3}$, U increases without bound. In practice, the solution will saturate once it reaches the peeling branch at $p_b \approx \Gamma^{1/2}\eta^{1/6}U^{1/3}$, a feature not included in (5.4).

To establish the accuracy of (5.4), we solved it numerically setting $p_b = 2.23$, $\Gamma = 0.5$. Figure 13(*a*) in Appendix B illustrates how U behaves in comparison to the

predictions of the asymptotic model. While no attempt was made to achieve quantitative accuracy, (5.4) shows how the delicate balance between the fluxes entering and leaving the volume $\mathscr{V}$ leads to bubble speeds that decay slightly quicker than $t^{-1/2}$, achieving this limit only at extremely large times. We show in Appendix B that the $t^{-1/2}$ behaviour is better captured by a similarity solution of the asymptotic model for which unsteady effects are retained throughout the inflated region ahead of the bubble tip, and that a more complex time-dependence (associated with the slow flux past the bubble tip) can be introduced to capture the evolution at earlier times.

On the basis of both the PDE and ODE models, we can interpret the evolution of the system under fixed p_b as a simple dynamical system. The two non-trivial steady solution branches (figure 2*a*) arise through a saddle–node bifurcation; the pushing solution acts like a saddle point, the peeling solution acts like a stable node. The trivial solution $U=0$ is also stable, attractive to all initial conditions if $p_\mathrm{b} < p_\mathrm{crit}$ and locally attractive for $p_\mathrm{b} < p_\mathrm{crit}$. In contrast, the dynamics when q_b is held fixed is much less straightforward.

5.4. *Unsteady motion at fixed* q_b

We can use (5.6) to understand the origin of the oscillatory instability identified in § 4.2.2. As described in § 4.2.2, the term $p_{\mathrm{b}t}L_1$ in (2.17), representing bubble volume changes associated with transverse bubble expansion, is necessary for the instability to arise. The ODE model reflects this: removing the equivalent term from (5.5) implies $q_\mathrm{b} = p_\mathrm{b}U/\Gamma$, and (5.6*a*) reduces to

$$U_t = -\frac{U^7}{q_\mathrm{b}^4\Gamma}\left(1-\frac{q_\mathrm{b}}{U^{1/3}}\right). \tag{5.10}$$

The fixed point $U=q_\mathrm{b}^3$ of (5.10) is now stable.

Restoring the critical term $p_{\mathrm{b}t}L_\mathrm{b}$ in (5.5), we first examine the linear stability of the solution of (5.6) representing a steadily propagating bubble: $U=q_\mathrm{b}^3$, $p_\mathrm{b}=\Gamma/q_\mathrm{b}^2$, $L_\mathrm{b}=q_\mathrm{b}^3 t$. An analysis of perturbations of this time-dependent base state (Appendix C) indicates that the instability develops when $L=O(\Gamma/q_\mathrm{b}^{11})$ and $t=O(\Gamma/q_\mathrm{b}^{14})$; thus the smaller q_b, the longer the instability takes to initiate. For $t \gg \Gamma/q_\mathrm{b}^{14}$, perturbations diverge from the base state along $p_\mathrm{b} \approx \Gamma/q_\mathrm{b}^2$. This is illustrated in the phase portrait in figure 14 in Appendix C. Because the base state is time-dependent, the initial instability cannot be classified in simple terms (it is a dynamic bifurcation of a non-autonomous system); somewhat surprisingly, the analysis in Appendix C shows that linearized perturbations ultimately grow monotonically rather than having an oscillatory character.

The behaviour of perturbations after they move away from the steady solution branch in the (p_b, U)-plane is illustrated in figure 12(*a*). Here we integrated (5.6) with $\Gamma=0.5$, $\eta=100$ and $q_\mathrm{b}=0.65$, starting from immediately beneath $(p_\mathrm{c}, U_\mathrm{c})$; each trajectory leaving this point follows a looping path beneath the steady pushing solution that ultimately brings it back up to the peeling solution branch; we then used (5.8) to track the motion back down the peeling branch. Around each loop L_b increases significantly, as shown in figure 12(*c*), while U and p_b perform nonlinear growing relaxation oscillations (figure 12*b*, *d*). There is good qualitative agreement with the computational simulations shown in figure 9, suggesting that this simple model captures well the dominant features of the instability. The ODE model allows us to simulate multiple growing oscillations and to estimate the rate at which the system evolves over very long time scales.

The sequence of events during an oscillation becomes clear once the bubble is very long. In this limit, a detailed asymptotic analysis of (5.6), presented in Appendix D for

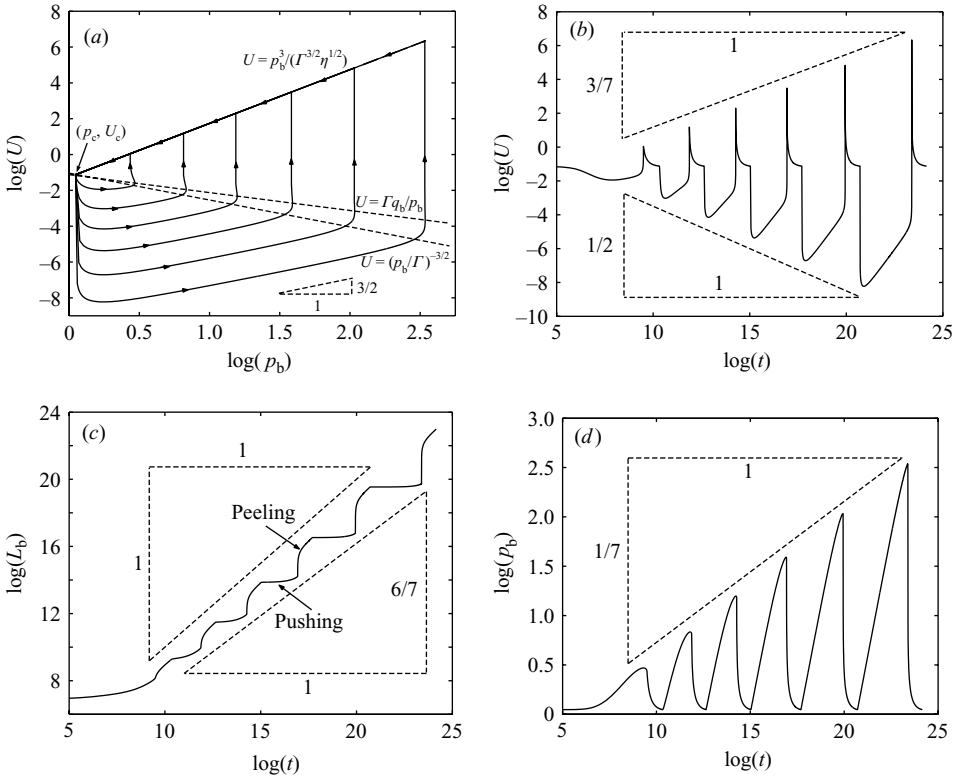

FIGURE 12. Numerical solution of (5.6) and (5.8), with $q_b = 0.65$, $\Gamma = 0.5$, $\eta = 100$ and $L_b(0) = 10^3$, showing (*a*) (p_b, U)-phase portrait; (*b*) U versus t; (*c*) L_b versus t and (*d*) p_b versus t. The turning point (p_c, U_c) lies at $(1.05, 0.33)$; the fixed point representing the steady pushing solution at this flux lies at $(p_b, U) = (1.18, 0.27)$, the intersection of the lines $U = \Gamma q_b/p_b$ and $U = (p_b/\Gamma)^{-3/2}$ in (*a*).

$L_b \gg 1$, shows how different balances of terms operate during different phases of the oscillation, which we summarize here. Suppose $L_b = L_0 \gg 1$, say, on entering the pushing phase of an oscillation at (p_c, U_c). Initially U falls rapidly with $p \approx p_c$. In this phase the bubble grows by widening rather than lengthening, and $\mathscr{V}$ grows slowly by accumulating fluid from ahead of the bubble, losing negligible quantities past the meniscus. Widening of the bubble causes p_b to rise slowly. From (5.3) we see that, for fixed $\mathscr{V}$, an increase in p_b allows the bubble to travel faster, there being lower viscous dissipation in a wider channel. Thus U falls to a minimum value $U_{\min}(\propto L_0^{-1/2})$ before starting to rise along a path $U \propto p_b^{3/2}$ in the (p_b, U)-plane (figure 12*a*). Eventually U increases sufficiently to cross the steady solution branch $p_b = \Gamma U^{-2/3}$, at which point more fluid escapes past the meniscus than is swept up from ahead of the bubble. Correspondingly $\mathscr{V}$ starts to fall, from a maximum value of $O(L_0^{11/12})$, and U begins to rise rapidly. Shortly thereafter the system crosses the curve $\Gamma p_b = q_b U$, at which point p_b rises to a maximum value $p_{b\max}(\propto L_0^{1/6})$, beyond which bubble growth now occurs by lengthening rather than widening. The bubble then undergoes a rapid transition from pushing to peeling motion, with $p_b \approx p_{bmax}$ and U rising abruptly to the peeling branch, where it attains its maximum value $U_{\max}(\propto L_0^{1/2})$. The rapid rise reflects the existence of a finite-time singularity in (5.6). We can therefore identify (p_m, U_m) in (5.9) with $(p_{b\max}, U_{\max})$. It is shown in Appendix D that the duration of pushing is $L_0^{7/6}$,

and the change in L_b during pushing is $O(L_0^{11/12})$, which formally (for $L_0 \gg 1$) is small compared to L_0. This allows us to set $L_m \approx L_0$ in (5.8), (5.9).

The system then moves quasi-steadily back from (p_m, U_m) to (p_c, U_c) along the peeling branch. Since U is small during the majority of the pushing phase, but large during the peeling phase, the bubble elongates predominantly during peeling. $L_b(t)$ therefore has a clear 'staircase' shape at large times (figure 12*c*), with the bubble tip switching abruptly between 'sticking' (during pushing) and 'slipping' (during peeling). We can estimate the increase in bubble length during peeling by noting that for $L_0 \gg 1$, $p_m U_m \propto L_0^{2/3}$, so that (5.9) implies $L_c = O(L_0^{7/6})$. Likewise (5.8) reduces for large L_0 to $L_b U^{1/3} = L_0 U_{max}^{1/3}$, representing conservation of bubble volume assuming that fluxes due to q_b are negligible. This may be integrated to give

$$L_b^4 = L_0^4 + 4L_0^3 U_m (t - t_m), \tag{5.11}$$

assuming $t = t_m$ when $U = U_m$. Since $L_c \gg L_0$ when $t = t_c$, say, the duration of the peeling phase of the oscillation is therefore $t_c - t_m = O(L_0^{7/6})$, comparable to that of the pushing phase.

Having established the structure of an individual oscillation in terms of the length L_0 at the start of the pushing phase, we can finally describe the evolution of the system over multiple oscillations. Let $L_b^{(n)}$ be the bubble length at $t = t_c^{(n-1)}$, the start of the pushing phase of the nth oscillation. We have already established that $L_b^{(n)} \propto [L_b^{(n-1)}]^{7/6}$, which we may write as

$$\log L_b^{(n)} \approx \tfrac{7}{6} \log L_b^{(n-1)}, \tag{5.12a}$$

the constant of proportionality being negligible for sufficiently large $L_b^{(n)}$. The end of the pushing phase occurs at time $t_m^{(n)} = t_c^{(n-1)} + J[L_b^{(n)}]^{7/6}$ for some constant J. Assuming $t_m^{(n)} \gg t_c^{(n-1)}$, this implies

$$\log t_m^{(n)} \approx \tfrac{7}{6} \log L_b^{(n)}. \tag{5.12b}$$

Likewise the end of peeling, at time $t_c^{(n)}$, also satisfies (to leading order)

$$\log t_c^{(n)} \approx \tfrac{7}{6} \log L_b^{(n)}. \tag{5.12c}$$

In the $(\log t, \log L_b)$-plane, points defining the start of pushing lie at $(\log t_c^{(n-1)}, \log L_b^{(n)})$ for $n = 1, 2, \ldots$. From (5.12*a*, *c*), for large n these points lie on a line of slope 1, as shown in figure 12(*c*); likewise, points at the start of peeling at $(\log t_m^{(n)}, \log L_b^{(n)})$ lie (from (5.12*b*)) on a line of slope $\frac{6}{7}$. Since $U_m^{(n)} \propto [L_b^{(n)}]^{1/2}$, $U_{min}^{(n)} \propto [L_b^{(n)}]^{-1/2}$ and $p_m^{(n)} \propto [L_b^{(n)}]^{1/6}$ (Appendix D), the maxima along the curve in figure 12(*b*) at $(\log t_m^{(n)}, \frac{1}{2} \log L_b^{(n)})$ lie along a line of slope $\frac{3}{7}$, the minima at $(\log t_c^{(n-1)}, -\frac{1}{2} \log L_b^{(n)})$ lie along a line of slope $-\frac{1}{2}$ and the maxima in figure 12(*d*) at $(\log t_m^{(n)}, \frac{1}{6} \log L_b^{(n)})$ lie along a line of slope $\frac{1}{7}$. Thus the oscillations grow in a self-similar fashion. Averaging over oscillations, the bubble elongates roughly linearly in time, although excursions in bubble volume and pressure grow like $t^{3/7}$ and $t^{1/7}$ respectively.

6. Discussion

In this paper we have examined the unsteady behaviour of a model of airway reopening wherein elastically supported flexible walls occluded by a viscous fluid are separated and opened by the progression of a long bubble of air. Two approaches were used to simulate the model system numerically: a spatially two-dimensional

boundary-element method (BEM) and a one-dimensional asymptotic model. The BEM model computes the Stokes flow around the bubble tip and connects to a downstream region that is modelled using a lubrication approximation. The asymptotic model assumes that the membrane region near the tip is nearly parallel, allowing prior studies for the quasi-steady flow of a bubble in a weakly tapered channel (Halpern & Jensen 2002) to be exploited. Agreement between BEM and asymptotic simulations confirm that the flow around the bubble tip region is quasi-steady and that much of the unsteady motion is controlled by the liquid-filled region ahead of the bubble tip. We also developed a simple lumped-parameter (ODE) model that captures the dominant dynamics of the system.

As with all modelling investigations, approximations may limit the validity of the studies. In this study we assumed that the lining fluid had a constant surface tension and was Newtonian. However, pulmonary lining fluid contains surfactant, which dynamically alters the surface tension. Studies by Yap & Gaver (1998) indicate that surfactant transport modifies the reopening pressures; however, the 'pushing' and 'peeling' branches remain. We therefore expect that surfactant transport will not qualitatively modify the stability behaviour of the system. We have also assumed that the channel walls are supported by a linearly elastic bed. However, lung airways are nonlinearly compliant (discussed below), and are tethered to neighbouring airways. Parenchymal tethering will reduce the reopening pressures but should not change the general form of the response, as observed in Perun & Gaver (1995*a*). We thus do not expect that the general stability behaviour will be modified substantially by tethering.

In our studies, steady pressure-driven flow is characterized by a non-monotonic pressure–speed relationship (see figures 2*a* and 4). The low speed 'pushing' regime is characterized by a long fluid-filled region downstream of the bubble tip that is displaced by the moving meniscus. High-speed reopening is characterized by a large peeling angle at the meniscus tip, which produces a low pressure that holds the channel walls in apposition. We found the pushing branch to be unstable when p_b is fixed, with a positive pressure perturbation resulting in a migration of the system to the peeling branch, and a negative perturbation resulting in an ever-slowing bubble that accumulates liquid in the region ahead of the bubble. The peeling branch was found to be stable to both positive and negative perturbations. As anticipated from the steady solution structure, the system exhibits dynamical behaviour typical of that associated with a saddle–node bifurcation.

In contrast, when q_b is prescribed the dynamics of the system are quite different, for three important reasons. First, the flux–speed and flux–pressure relationships are now single-valued (figure 2*b*, *c*), precluding any obvious direct instabilities of steadily propagating solutions. Second, the system has an extra degree of freedom, since $p_b(t)$ now becomes a dependent variable. Third, the solutions shown in figure 2(*b*, *c*) are not strictly steady solutions of the problem, since they depend explicitly on bubble length, which increases with time. Our studies demonstrate that the peeling mode (with high q_b) is again stable. However, arbitrarily small perturbations of the pushing mode ultimately result in growing non-periodic oscillations (figures 9 and 10). Each oscillation has two distinct phases. During the pushing phase the bubble inflates predominantly by widening, its tip speed is very low, and it slowly accumulates fluid ahead of the tip. Once the bubble is sufficiently wide the tip suddenly pierces the accumulated fluid and there is an abrupt transition into the peeling phase, during which the bubble inflates by predominantly by lengthening and its tip travels quickly forwards. Subsequently, the slow pushing mode is restored and the cycle begins anew, albeit with greater oscillation amplitude and period.

This novel oscillatory instability arises through a global flow–bubble–structure interaction. We have isolated its origins to be the increasing upstream compliance as the bubble travels forward and leaves behind an increasing length of open channel. As the compliance increases, small fluctuations in p_b induce very large changes in bubble volume, allowing the bubble to switch spontaneously between pushing and peeling modes of reopening, resulting in an effective stick–slip motion (figure 12*c*). While the full problem is an infinite-dimensional dynamical system, we found that we could capture this non-periodic relaxation oscillation using a simple third-order ODE model. We showed that steady pushing motion (a solution having explicit time dependence in the ODE model) is linearly unstable to a direct instability at sufficiently large times (described using Kummer's functions, see Appendix C). The theory of non-autonomous dynamical systems does not yet appear sufficiently well developed (Langa, Robinson & Suárez 2002) for this type of instability to have been classified. The direct linear instability grows into an inherently nonlinear oscillation. We were able to provide a detailed analysis of the sequence of events during a large-amplitude oscillation (Appendix D), showing self-similarity between consecutive oscillations captured through a nonlinear map (5.12).

With a linearly elastic channel support, the stick–slip response has an ever-growing oscillation amplitude. Simplistically, bubble inflation occurs in two ways: with slowly increasing length and rapidly increasing width (slow pushing); or with nearly constant width and rapidly increasing length (quick peeling). We have shown that at a fixed flow rate in long linearly elastic channels, the system can spontaneously switch between these two states. However, true pulmonary airways are nonlinearly elastic structures, with a compliance that decreases as the internal pressure increases. We would thus not expect that oscillations would continuously grow in more realistic structures. For similar reasons, we do not expect to see the instability appear strongly in the membrane-between-plates configuration, since the plates prevent transverse bubble expansion. Our previous simulations of the membrane-between-plates model exhibited overshoot upon startup, but did not exhibit instability, at least for the range of parameters we investigated (Naire & Jensen 2003). Experiments demonstrate similar startup responses, but do not exhibit obvious oscillations (Perun & Gaver 1995*b*). However, slow reopening in a flow-rate-driven system with an elastically supported membrane between rigid plates did exhibit unstable behaviour at low speeds, typically by an ever-slowing bubble tip. It is possible that this represents the onset of a peeling-to-pushing response (Perun & Gaver 1995*a*).

The oscillatory response of the flow-based system is intriguing, and we speculate that this response may explain (in part) the 'avalanche' reopening of sequential airways described by Suki *et al.* (1994). To explore this behaviour, recent experiments by Alencar *et al.* (2002) investigated the inflation of isolated, degassed rat lungs that were inflated at a constant flow rate. These studies show that the pressure increases and then exhibits intermittent regions of decreasing pressure, similar to that shown in figure 10(*b*). The oscillatory variation of pressure was interpreted as coinciding with an avalanche of airway reopening, which rapidly increases the volume of the open region of the lung. While the present model is incapable of replicating the complexities of the whole lung response, the behaviour reported in Alencar *et al.* (2002) may be related to the instabilities observed in our constant-flow studies. In this case, the patent region of the lung provides the upstream compliance for the system, thus providing a mechanism for the *pendelluft*-like behaviour that induces oscillations similar to that observed in our models. As described above, because of the nonlinear compliance of the lung, we would not expect the oscillation magnitude to grow without bound.

Future studies may be able to determine whether the responses observed *in vitro* are consistent with present models.

This work was supported by EPSRC grant GR/M84572 and GR/R08292/01, NASA grant NAG3-2734, NIH grant P20 EB001432-01, NSF grant BES-9978605 and Wellcome Trust grant 061142. We wish to acknowledge the contributions of Mark Horsburgh to the early stages of this work.

Appendix A. Regression formulae

The following regression formulae are used for $U > 0.01$:

$$\begin{aligned}\lambda_0 &= 0.417(1-\exp(-1.69U^{0.5025})),\\ \log_{10}(-\mathscr{P}_0) &= -2.00858 + 8.92426\exp(-0.038332(Z+5)^{2.17398}) + 0.898217Z,\\ \lambda_1 &= 0.0769 - 0.04119z - 4.63\times10^{-3}z^2 + 4.46\times10^{-3}z^3\\ &\quad + 2.47442\times10^{-4}z^4 - 2.12954\times10^{-4}z^5 - 2.51264\times10^{-5}z^6,\end{aligned}$$

where $Z = \log_{10}(U)$ and $z = \log(U)$. For $U < 0.01$, we use the asymptotic expressions $\lambda_0 = \lambda_1 \approx 1.337U^{2/3}$, $U\mathscr{P}_0 \approx -1 - 3.80U^{2/3}$. Graphs of these functions may be found in Jensen *et al.* (2002).

Appendix B. Quasi-self-similar large-time pushing motion

Figure 13(*a*), computed using the asymptotic model, shows the large-time evolution of an unsteady pushing solution. Over extremely long times, the scaling $U \sim T^{-1/2}$ is evident, a feature captured by the ODE model (5.4).

Setting $\xi = X/T^{1/2}$ and $U = U/T^{1/2}$, and assuming $H = H(\xi)$, (3.5) and (3.7) become, with error $o(T^{-1/3})$,

$$\tfrac{1}{2}\xi H_\xi + UH_\xi + \tfrac{1}{3}\delta^2(H^3H_\xi)_\xi = 0, \tag{B 1}$$

subject to the boundary conditions at $\xi = 0$,

$$\delta^2(H_\mathrm{b}-1) - \delta P_\mathrm{b} = -\epsilon/H_\mathrm{b}, \tag{B 2a}$$

$$H_\mathrm{b}\left(U + \tfrac{1}{3}\delta^2H_\mathrm{b}^2H_\xi\right) = \alpha U^{5/3}T^{-1/3}, \tag{B 2b}$$

and $H \to 1$ as $\xi \to \infty$. We have used $U\mathscr{P} \to -1$ and $\lambda = \alpha U^{2/3}$ as $U \to 0$ in (B 2*a*) and (B 2*b*), where $\alpha \approx 1.337$ (Bretherton 1961). We neglect the $O(T^{-1/3})$ flux past the bubble in (B 2*b*) to start with, but anticipate that it could be retained as a quasi-steady boundary condition. Note that we cannot apply the slope boundary condition (3.7*a*) since membrane tension does not appear at leading order in (B 1).

The problem may be simplified by rescaling, setting $\xi = (\delta/\sqrt{3})Z$ and $U = (\delta/\sqrt{3})V$, so that (B 1) and (B 2) reduce to

$$\tfrac{1}{2}ZH_Z + VH_Z + (H^3H_Z)_Z = 0, \tag{B 3a}$$

$$P_\mathrm{b} = \delta(H_\mathrm{b}-1) + \epsilon/(\delta H_\mathrm{b}), \tag{B 3b}$$

$$V + H_\mathrm{b}^2H_Z = \alpha(\delta^2/3)^{1/3}V^{5/3}T^{-1/3}, \tag{B 3c}$$

$$H \to 1 \ \text{ as } \ Z \to \infty. \tag{B 3d}$$

The solution strategy is as follows. For $Z \to \infty$, solutions of (B 3*a*) can be written as

$$H \sim 1 + \mathscr{A}\sqrt{\pi}\,\mathrm{e}^{V^2}\mathrm{erfc}\left(\tfrac{1}{2}Z + V\right). \tag{B 4}$$

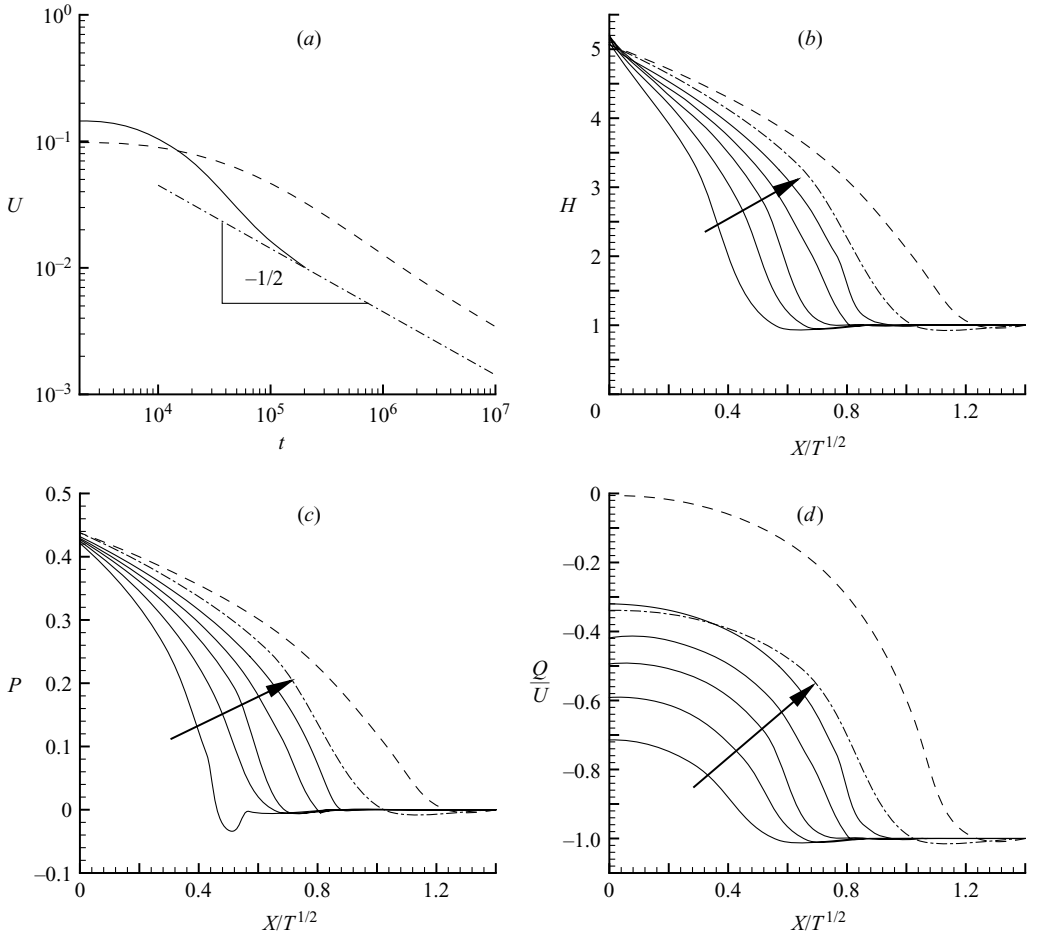

FIGURE 13. (*a*) U versus T (solid), computed using the asymptotic model, showing the $T^{-1/2}$ scaling at very long times; the dashed curve shows a solution of (5.4). (*b–d*) Profiles of H, P and Q/U versus $\xi = X/T^{1/2}$, with $p_b = 2.23$, $\epsilon = 0.215$, $\delta = 0.328$, $T = (5, 8, 13, 20, 30) \times 10^3$; the dashed curve shows the infinite-time similarity solution, the dot-dashed curve shows the quasi-self-similar solution at $T = 30000$.

For fixed V and T, one can shoot with Z decreasing to 0, and vary $\mathscr{A}$ until (B 3*c*) is satisfied. Then we read off the corresponding value of P_b from (B 3*b*). The choice of V is then adjusted to obtain the required value of P_b.

Large-time solutions of the asymptotic model are plotted versus $X/T^{1/2}$ in figure 13(*b–d*), in the case $p_b = 2.23$, along with the infinite-time similarity solution (for which $V \approx 8.0$). Even for T well in excess of 10000, the infinite-time solution does not match well to solutions of the PDEs, nor do the PDE solutions collapse particularly well when plotted in rescaled variables. However, by including the quasi-steady flux past the bubble tip, much improved agreement is obtained; this is shown by computing the quasi-self-similar solution at $T = 30000$, for which we found $V \approx 10.2$. The effects of tension, neglected in the similarity solution, are confined to a small damped wave at the leading edge of the advancing disturbance and a weak boundary layer near $X = 0$ giving rise to a small adjustment in the membrane slope ahead of the bubble tip.

Appendix C. Stability of the pushing solution to small perturbations

Writing $U = p_b^4 W$, (5.6*a–c*) become

$$W_t = -\Gamma^3 p_b^4 W^3 \left(1 - p_b^{11/3} W^{2/3}/\Gamma\right), \tag{C 1a}$$

$$p_{bt} = \left(\Gamma q_b - p_b^5 W\right)/L_b, \tag{C 1b}$$

$$L_{bt} = p_b^4 W. \tag{C 1c}$$

The equations have a base state for which p_b and W are constant but L_b increases steadily with t. We perturb around this solution by writing

$$p_b = \frac{\Gamma}{q_b^2} + \frac{\Gamma^5}{q_b^{13}}\tilde{p}_b, \quad W = \frac{q_b^{11}}{\Gamma^4} + \tilde{W}, \quad t = \frac{\Gamma}{q_b^{14}}\tilde{t}, \quad L_b = \frac{\Gamma}{q_b^{11}}\tilde{L}_b. \tag{C 2}$$

Assuming that $\tilde{L}_b$ and $\tilde{t}$ are $O(1)$ and that either $\tilde{p}_b$ and $\tilde{W}$ are small or $\tilde{p}_b$ and $\tilde{W}$ are $O(1)$ and $q_b \gg \Gamma^{11/4}$, (C 1) becomes

$$\tilde{W}_{\tilde{t}} = \tfrac{2}{3}\tilde{W} + \tfrac{11}{3}\tilde{p}_b, \tag{C 3a}$$

$$\tilde{p}_{b\tilde{t}} = -(\tilde{W} + 5\tilde{p}_b)/\tilde{L}_b, \tag{C 3b}$$

$$\tilde{L}_{b\tilde{t}} = 1. \tag{C 3c}$$

Integrating (C 3*c*) to give $\tilde{L}_b = \tilde{L}_{b0} + \tilde{t}$ for some constant $\tilde{L}_{b0}$, (C 3*a*, *b*) can be re-expressed as the second-order system

$$\tilde{W}_{\tilde{t}\tilde{t}} + \left(\frac{5}{\tilde{t} + \tilde{L}_{b0}} - \frac{2}{3}\right)\tilde{W}_{\tilde{t}} + \frac{1}{3(\tilde{t} + \tilde{L}_{b0})}\tilde{W} = 0. \tag{C 4}$$

The transformation $\tilde{t} + \tilde{L}_{b0} = \frac{3}{2}T$ gives $T\tilde{W}_{TT} + (5 - T)\tilde{W}_T + \frac{1}{2}\tilde{W} = 0$, which is Kummer's equation (Abramowitz & Stegun 1965), the general solution of which is $\tilde{W} = AM^K(T) + BU^K(T)$ for constants A and B. Here we use the special functions $M^K(T) \equiv M(-\frac{1}{2}, 5, T)$ and $U^K(T) \equiv U(-\frac{1}{2}, 5, T)$. Note that $M^K(T) \sim 1 - \frac{1}{10}T$, $U^K(T) \sim -3/(\sqrt{\pi}T^4)$ as $T \to 0$, and $M^K(T) \propto T^{-11/2}\mathrm{e}^T$, $U^K(T) \sim T^{1/2}$ as $T \to \infty$. Figure 14(*a*) illustrates some characteristic curves in the phase-plane diagram of $\tilde{W}$ versus $\tilde{p}_b$. The corresponding time evolution of $\tilde{W}$ is shown in figure 14(*b*). For $T \ll 1$, both $\tilde{W}$ and $\tilde{p}_b$ decay rapidly in magnitude. This is because contributions in $\tilde{W}$ and $\tilde{p}_b$ proportional to U^K decay rapidly while those proportional to M^K are almost constant. This indicates that the base states are attractive at early times. However, as T increases the contributions of $\tilde{W}$ and $\tilde{p}_b$ proportional to M^K grow rapidly and ultimately dominate (figure 14*b*), demonstrating instability of the base state. For $T \gg 1$, $\tilde{W}(\propto \tilde{T}^{-11/2}\mathrm{e}^{\tilde{T}})$ grows more rapidly than $\tilde{p}_b(\propto \tilde{T}^{-13/2}\mathrm{e}^{\tilde{T}})$.

Appendix D. Asymptotics of the ODE model for pushing motion

Equation (5.6) may be simplified when the bubble is long, since during pushing motion U is small and so changes in L_b may be neglected to leading order. We set $L_b = L_0 + \hat{L}_0(t)$, where $|\hat{L}_0| \ll L_0$. Then (5.6) may be written as $\hat{L}_{0t} = U$ and

$$U_t = \frac{4U}{p_b L_0}(\Gamma q_b - p_b U) - \frac{\Gamma^3 U^3}{p_b^4}\left(1 - \frac{p_b}{\Gamma}U^{2/3}\right), \tag{D 1a}$$

$$p_{bt} = (\Gamma q_b - p_b U)/L_0. \tag{D 1b}$$

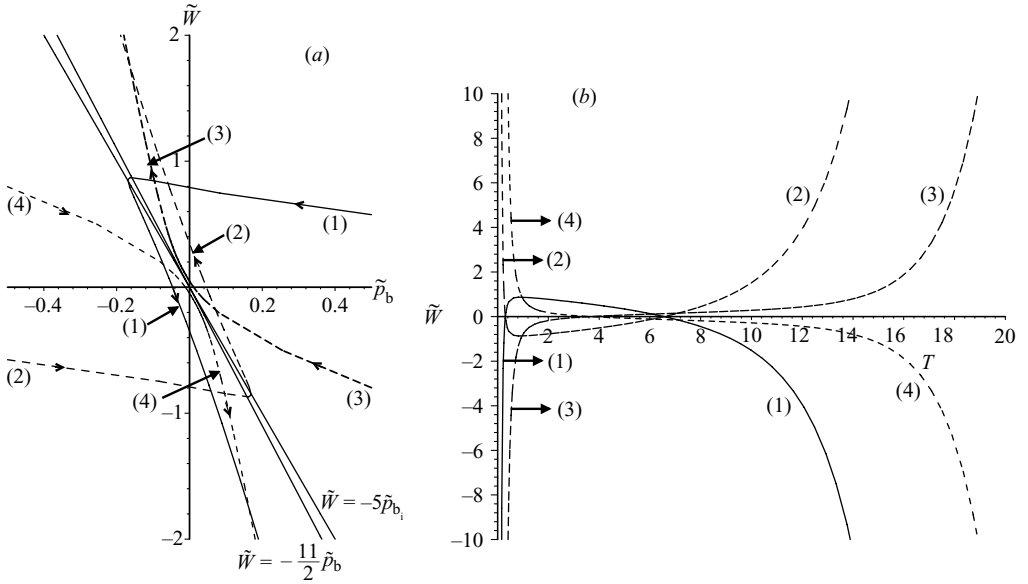

FIGURE 14. (*a*) Phase-plane diagram of $\tilde{W}$ versus $\tilde{p}_b$ showing four trajectories labelled (1)–(4) and the nullclines $\tilde{W} = -11\tilde{p}_b/2$ and $\tilde{W} = -5\tilde{p}_b$; (*b*) corresponding evolution of $\tilde{W}$ versus T.

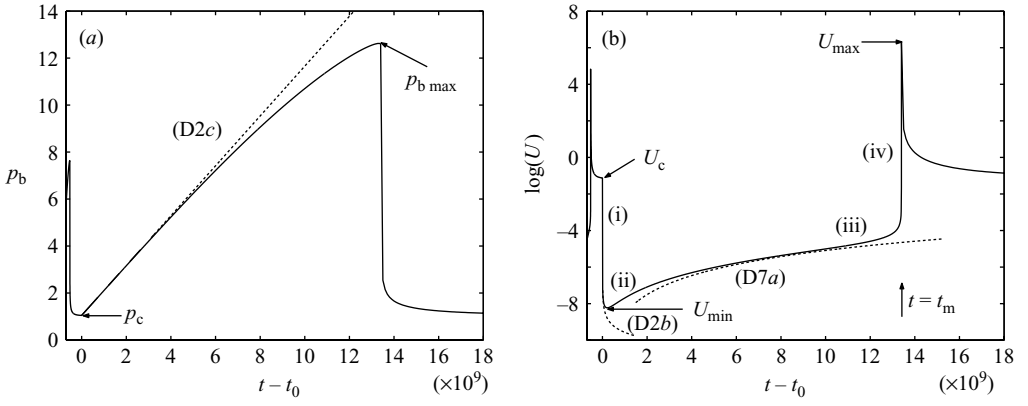

FIGURE 15. Time evolution of (*a*) p_b and (*b*) U during the sixth oscillation of figure 12. The dashed curves correspond to the asymptotic solutions (D2*b*, *c*) and (D7*a*); parameter values are $t_0 \approx 9.9 \times 10^8$, $L_0 \approx 3 \times 10^8$, $p_c = 1.05$, $\Gamma = 0.5$ and $q_b = 0.65$.

This system now permits an asymptotic analysis, taking $1/L_0$ as a small parameter. The motion has distinct temporal phases that we analyse in turn, as illustrated in figure 15.

(i) *Sudden slowing*. As long as $p_b U = O(1)$, for $L_0 \gg 1$ changes in p_b are small, and the evolution of U is equivalent to that for which p_b is prescribed. Thus if U lies just below the steady solution branch $p_b = \Gamma U^{-2/3}$, the dynamics initially follow (5.4) with constant p_b. Linearizing (5.4) around the steady solution (Appendix C) shows that U initially falls from its steady value exponentially on a time scale p_b^7/Γ^6, i.e. Γ/q_b^{14} if evolving from the steady pushing solution, or p_c^7/Γ^6 is evolving from the turning point of the two steady solution branches. We focus here on the latter case,

taking $p_b \approx p_c$. Thus U rapidly falls to low values, being governed (once U is small) by $U_t \approx -\Gamma^3 U^3/p_c^4$. Meanwhile, p_b starts to rise slowly via (D 1*b*), so that for $t > t_0$ for some constant t_0

$$L \approx L_0 + \left(\frac{2p_c^4}{\Gamma^3}(t-t_0)\right)^{1/2}, \quad U \approx \left(\frac{p_c^4}{2\Gamma^3(t-t_0)}\right)^{1/2}, \quad p_b \approx p_c + \frac{\Gamma q_b}{L_0}(t-t_0). \tag{D 2}$$

The sudden fall in U and the slow rise in p_b in (D 2*b*, *c*) compare favourably to a solution of (5.6) in figure 15(*b*). Once $t - t_0 = O(L_0 p_c/q_b\Gamma)$, this approximation breaks down.

To analyse subsequent behaviour we first reduce (D 1*a*, *b*) to the first-order system

$$\frac{\mathrm{d}U}{\mathrm{d}p_b} = \frac{4U}{p_b} - \frac{\Gamma^3 U^3 L_0}{p_b^4}\frac{\left(1 - p_b U^{2/3}/\Gamma\right)}{(\Gamma q_b - p_b U)}. \tag{D 3}$$

Setting $U = p_b^4 W(p_b)$ and $\alpha = \Gamma^2 L_0/q_b$, (D 3) becomes

$$\frac{\mathrm{d}W}{\mathrm{d}p_b} = -\alpha W^3 p_b^4 \frac{\left(1 - p_b^{11/3} W^{2/3}/\Gamma\right)}{\left(1 - p_b^5 W/(\Gamma q_b)\right)}. \tag{D 4}$$

Equation (D 4) relates pressure to volume, since $W = 1/(\Gamma^3 \mathscr{V})$, where $\mathscr{V}$ is the fluid volume ahead of the bubble (figure 11). For $\alpha \gg 1$, the trajectory in the (p_b, W)-plane has three further phases.

(ii) *Minimum speed*. We first set $W = \alpha^{-1/2} W_1$, $p_b = p_1$, and assume W_1 and p_1 are $O(1)$ variables. Then (D 4) becomes

$$\frac{\mathrm{d}W_1}{\mathrm{d}p_1} = -W_1^3 p_1^4 \frac{\left(1 - p_1^{11/3} W_1^{2/3}/\left(\Gamma\alpha^{1/3}\right)\right)}{\left(1 - p_1^5 W_1/\left(\Gamma q_b \alpha^{1/2}\right)\right)}. \tag{D 5}$$

At leading order, $\mathrm{d}W_1/\mathrm{d}p_1 \approx -W_1^3 p_1^4$, which has the solution

$$W_1^2 = \frac{5}{2\left(p_1^5 - p_c^5\right)}, \tag{D 6}$$

imposing the boundary condition $W_1 \to \infty$ as $p_1 \to p_c +$; in this limit (D 6) matches with (D 2). In the original variables, (D 6) is $U^2 = 5p_b^8/(2\alpha(p_b^5 - p_c^5))$, which has a turning point in the (p_b, U)-plane at $p_b = p_c(8/3)^{1/5}$, $U = U_{\min} \equiv \alpha^{-1/2} p_c^{3/2} 2(8/3)^{3/10}$. Using the parameter values in figure 15, this predicts $\log U_{\min} \approx -8.22$, in close agreement with the ODE solution.

As p_1 increases well beyond p_c, (D 6) asymptotes to $W_1^2 \approx 5/(2p_1^5)$. During this stage,

$$U \approx \left(\frac{5\Gamma}{2}\right)^{1/2} \frac{q_b^2}{L_0^2}(t-t_0)^{3/2}, \quad p_b \approx \frac{\Gamma q_b}{L_0}(t-t_0). \tag{D 7}$$

The scaling $U \propto p_b^{3/2}$ is demonstrated in figure 12, and (D 7*a*) compares well with the ODE solution in figure 15(*b*).

(iii) *Maximum volume*. The next phase arises as the system crosses the steady pushing solution branch (see figure 12*a*). To describe this, we set $W_1 = \alpha^{-5/12} W_2$, $p_1 = \alpha^{1/6} p_2$, and now treat W_2 and p_2 as $O(1)$ variables. Equation (D 5) becomes

$$\frac{\mathrm{d}W_2}{\mathrm{d}p_2} = -W_2^3 p_2^4 \frac{\left(1 - p_2^{11/3} W_2^{2/3}/\Gamma\right)}{\left(1 - p_2^5 W_2/\left(\Gamma q_b \alpha^{1/12}\right)\right)}. \tag{D 8}$$

Without the $\alpha^{-1/12}$ term, which is negligible for sufficiently large L_0, (D 8) captures a turning point in the (p_2, W_2)-plane. For $p_2 \to 0$, (D 8) has the asymptotic solution $W_2^2 \approx 5/(2p_2^5)$. Beyond the turning point, as W_2 grows, the dynamics are described by $\mathrm{d}W_2/\mathrm{d}p_2 \approx W_2^{11/3} p_2^{23/3}/\Gamma$. This has the solution

$$W_2^{-8/3} = \frac{8}{26\Gamma}\left(p_{2\star}^{26/3} - p_2^{26/3}\right) \tag{D 9}$$

for some constant $p_{2\star}$, implying that $W_2 \to \infty$ as $p_2 \to p_{2\star}-$. Using (D 7), the time $t^\star$ at which p_2 approaches $p_{2\star}$ is given to leading order by

$$t^\star = t_0 + \left(\frac{L_0^7}{q_\mathrm{b}^7 \Gamma^4}\right)^{1/6} p_{2\star}. \tag{D 10}$$

As p_2 rises linearly in t towards $p_{2\star}$, U rises abruptly like $(t^\star - t)^{-3/8}$.

(iv) *Maximum pressure*. The blowup in (D 9) is mediated by the denominator of (D 8), which becomes important during the final phase of pushing motion. Here, we set

$$p_2 = p_{2\star} + \Gamma^{-5/3} q_\mathrm{b}^{-8/3} \alpha^{-2/9} p_{2\star}^{17/3} p_3, \qquad W_2 = \Gamma q_\mathrm{b} \alpha^{1/12} p_{2\star}^{-5} W_3, \tag{D 11}$$

now treating p_3 and W_3 as $O(1)$ variables. Equation (D 8) becomes, to leading order for $\alpha \gg 1$,

$$\frac{\mathrm{d}W_3}{\mathrm{d}p_3} = \frac{W_3^{11/3}}{1 - W_3}, \tag{D 12}$$

which has the solution

$$p_3 - p_{3\star} = \tfrac{3}{5} W_3^{-5/3} - \tfrac{3}{8} W_3^{-8/3} \tag{D 13}$$

for some $O(1)$ constant $p_{3\star}$. As $W_3 \to 0$ in (D 13), the balance $p_3 \approx -\frac{3}{8} W_3^{-8/3}$ matches with (D 9); at this stage, p_b continues to increase linearly with t towards $t^\star$ as in (D 7*b*), while $U \propto (t^\star - t)^{-3/8}$. As t approaches $t^\star$, p_b passes through its maximum value ($p_{b\,\max}$, say) and then falls slightly according to (D 13), while U continues to increase abruptly. Thus to leading order,

$$p_{b\,\max} = (\Gamma^2 L_0/q_\mathrm{b})^{1/6} p_{2\star} + O\left(L_0^{-2/9}\right), \tag{D 14}$$

where $p_{2\star}$ is an $O(1)$ constant. Once W_3 becomes large, $p_3 \approx p_{3\star} + \frac{3}{5} W_3^{-5/3}$. At this stage U grows according to $U_t = \Gamma^2 U^{11/3}/p_{b\,\max}^3$ (see (D 1*a*)), so that $U \propto (t_\mathrm{m} - t)^{-3/8}$, $p_{b\,\max} - p_\mathrm{b} \propto (t_\mathrm{m} - t)^{5/8}$ and $L_\mathrm{m} - L \propto (t_\mathrm{m} - t)^{5/8}$, where L_m and $t_\mathrm{m} (\approx t^\star)$ denote the length and time at the end of the pushing phase.

In conclusion, during the pushing phase, U falls to a minimum value $U_{\min} \propto L_0^{-1/2}$, p_b rises to a maximum value $p_{b\,\max} \propto L_0^{1/6}$ and the pushing phase lasts a time $O(L_0^{7/6})$. Simulations confirm that the largest change in bubble length occurs predominantly during the period in which U and p_b satisfy (D 7). Since $L_t \propto (t - t_0)^{3/2}/L_0^2$ while $t - t_0 = O(L_0^{7/6})$, the change in length during the oscillation $\Delta L = O(L_0^{11/12})$. Thus $\Delta L/L_0 \to 0$ in the limit $L_0 \to \infty$, consistent with the original approximation that L_0 may be assumed constant, although L_0 must obviously be very large to ensure $L_0^{-1/12}$ is numerically small.

REFERENCES

Abramowitz, M. & Stegun, I. 1965 *Handbook of Mathematical Functions*. Dover.

Alencar, A. M., Arold, S. P., Buldyrev, S. V., Majumdar, A., Stamenovic, D., Stanley, H. E. & Suki, B. 2002 Physiology: Dynamic instabilities in the inflating lung. *Nature* **417**, 809–811.

Bilek, A. M., Dee, K. C. & Gaver, D. P., III. 2003 Mechanisms of surface-tension-induced epithelial cell damage in a model of pulmonary airway reopening. *J Appl. Physiol.* **94** (2), 770–783.

Bretherton, F. 1961 The motion of long bubbles in tubes. *J. Fluid Mech.* **10**, 166–188.

Gaver III, D. P., Halpern, D., Jensen, O. E. & Grotberg, J. B. 1996 The steady motion of a semi-infinite bubble through a flexible-walled channel. *J. Fluid Mech.* **319**, 25–65.

Gaver III, D. P., Jensen, O. E. & Halpern, D. 2005 Surfactant and airway liquid flows. In *Molecular Mechanisms in Lung Surfactant (dys) function* (ed. K. Nag). Marcel Dekker (in press).

Gaver III, D. P., Samsel, R. W. & Solway, J. 1990 Effects of surface tension and viscosity on airway reopening. *J. Appl. Physiol.* **69** (1), 74–85.

Grotberg, J. B. 1994 Pulmonary flow and transport phenomena. *Annu. Rev. Fluid Mech.* **26**, 529–571.

Grotberg, J. B. 2001 Respiratory fluid mechanics and transport processes. *Annu. Rev. Biomed. Engng* **3**, 421–457.

Guyer, B., Hoyert, D. L., Martin, J. A., Ventura, S. J., MacDorman, M. F. & Strobino, D. M. 1999 Annual summary of vital statistics–1998. *Pediatrics* **104** (6), 1229–1246.

Halpern, D. & Grotberg, J. B. 1992 Fluid-elastic instabilities of liquid-lined flexible tubes. *J. Fluid Mech.* **244**, 615–632.

Halpern, D. & Jensen, O. E. 2002 The motion of a semi-infinite bubble in a covergent channel. *Phys. Fluids* **14**, 431–442.

Hazel, A. & Heil, M. 2003 Three-dimensional airway reopening: The steady propagation of a semi-infinite bubble into a buckled elastic tube. *J. Fluid Mech.* **478**, 47–70.

Heil, M. 1999*a* Airway closure: occluding liquid bridges in strongly buckled elastic tubes. *Trans. ASME J. Biomech. Engng* **121**, 487–493.

Heil, M. 1999*b* Minimal liquid bridges in non-axisymmetrically buckled elastic tubes. *J. Fluid Mech.* **380**, 309–337.

Heil, M. 2000 Finite Reynolds number effects in the propagation of an air finger into a liquid-filled flexible-walled Channel. *J. Fluid Mech.* **424**, 21–44.

Heil, M. & White, J. 2002 Airway closure: surface-tension-driven non-axisymmetric instabilities of liquid-lined elastic rings. *J. Fluid Mech.* **462**, 79–109.

Hindmarsh, A. C. 1982 Odepack, a systematized collection of Ode solvers. In *Scientific Computing* (ed. R. S. Stepleman *et al.*), *IMACS Transactions on Scientific Computation*, vol. 1, pp. 55–64. North-Holland.

Horsburgh, M. K. 2000 Bubble propagation in flexible and permeable channels. PhD thesis, University of Cambridge.

Howell, P. D., Waters, S. L. & Grotberg, J. B. 2000 The propagation of a liquid bolus along a liquid-lined flexible tube. *J. Fluid Mech.* **406**, 309–335.

Hsu, S.-H., Strohl, K. & Jamieson, A. 1994 Role of viscoelasticity in tbe tube model of airway reopening i. nonnewtonian sols. *J. Appl. Physiol.* **76** (6), 2481–2489.

Jensen, O. E. & Horsburgh, M. K. 2004 Modelling the reopening of liquid-lined lung airways. In *Wall/Fluid Interactions in Physiological Flows* (ed. M. Collins & M. Atherton). WIT Press.

Jensen, O. E., Horsburgh, M. K., Halpern, D. & Gaver III, D. P. 2002 The steady propagation of a bubble in a flexible-walled channel: asymptotic and computational models. *Phys. Fluids* **14**, 443–457.

Johnson, M., Kamm, R. D., Ho, L. W., Shapiro, A. H. & Pedley, T. J. 1991 The nonlinear growth of surface-tension-driven instabilities of a thin annular film. *J. Fluid Mech.* **233**, 141–156.

Kamm, R. D. & Schroter, R. C. 1989 Is airway closure caused by a liquid film instability? *Resp. Physiol.* **75**, 141–156.

Langa, J. A., Robinson, J. C. & Suárez, A. 2002 Stability, instability, and bifurcation phenomena in non-autonomous differential equations. *Nonlinearity* **15**, 887–903.

Naire, S. & Jensen, O. E. 2003 An asymptotic model of unsteady airway reopening. *Trans. ASME J. Biomech. Engng* **125**, 823–831.

Notter, R. H. 2000 *Lung Surfactants — Basic Science and Clinical Applications*, 1st Edn., *Lung Biology in Health and Disease*, vol. 149. Marcel Dekker, Inc.

Perun, M. L. & Gaver, D. P. 1995*a* An experimental model investigation of the opening of a collapsed untethered pulmonary airway. *Trans. ASME J. Biomech. Engng* **117**, 245–253.

Perun, M. L. & Gaver, D. P. 1995*b* Interaction between airway lining fluid forces and parenchymal tethering during pulmonary airway reopening. *J. Appl. Physiol.* **79**, 1717–1728.

Rosenzweig, J. & Jensen, O. E. 2002 Capillary-elastic instabilities of liquid-lined lung airways. *Trans. ASME J. Biomech. Engng* **124**, 650–655.

Savla, U., Sporn, P. H. & Waters, C. M. 1997 Cyclic stretch of airway epithelium inhibits prostanoid synthesis. *Am. J. Physiol.* **273** (5 Pt 1), L1013–9.

Suki, B., Alencar, A. M., Sujeer, M. K., Lutchen, K. R., Collins, J. J., Andrade, J. S., J., Ingenito, E. P., Zapperi, S. & Stanley, H. E. 1998 Life-support system benefits from noise. *Nature* **393**, 127–128.

Suki, B., Barabasi, A.-L., Hantos, Z., Petak, F. & Stanley, H. 1994 Avalanches and power-law behaviour in lung inflation. *Nature* **368**, 615–618.

Tschumperlin, D. J., Oswari, J. & Margulies, A. S. 2000 Deformation-induced injury of alveolar epithelial cells. effect of frequency, duration, and amplitude. *Am. J. Respir. Crit. Care Med.* **162** (2 Pt 1), 357–362.

Yap, D. Y. K. & Gaver, D. P. 1998 The influence of surfactant on two-phase flow in a flexible-walled channel under bulk equilibrium conditions. *Phys. Fluids* **10**, 1846–1863.